University of Nevada, Reno

Towards 3D Crop Phenotyping of Above- and Belowground Grain Sorghum Plant Traits Using Airborne Mounted Multispectral Camera, TLS, and GPR Remote Sensing Technologies

A Thesis submitted in partial fulfillment of the requirement for the degree of

Master of Science in Animal & Rangeland Sciences

Submitted by

Russell Godkin

Robert A. Washington-Allen, Ph.D. (Major Advisor)

May 2023

N

THE GRADUATE SCHOOL

We recommend that the thesis
prepared under our supervision by

RUSSELL GODKIN

entitled

**Towards 3D Crop Phenotyping of Above- and Belowground
Grain Sorghum Plant Traits Using Airborne Mounted
Multispectral Camera, TLS, and GPR Remote Sensing
Technologies**

be accepted in partial fulfillment of the
requirements for the degree of

Master of Science

Robert Washington-Allen
Advisor

Melinda K. Yerka
Committee Member

John N. Louie
Graduate School Representative

Markus Kemmelmeier, Ph.D., Dean
Graduate School

May, 2023

Abstract

Remote sensing technologies are increasingly used in agriculture, primarily focusing on crop phenotyping and nondestructive plant health monitoring. Climate change in the western United States has led to increasing aridity, and reduced precipitation and thus a growing need for emerging varieties of drought-tolerant crops and technology to accurately monitor their establishment. Remote sensing technologies have the capability of efficiently fulfilling this need. The utilization of terrestrial laser scanning (TLS), ground penetrating radar (GPR) and small unoccupied aerial vehicles (sUAS) allow us to monitor and assess plant traits and health metrics. These three technologies were employed during the 2021 and 2022 growing seasons of two varieties of drought-tolerant grain sorghum (*Sorghum Bicolor* L. Moench) under deficit irrigation. The red and white varieties of sorghum were monitored using a randomized split plot design with three levels of deficit irrigation (30%, 60%, and 100%). These plots were replicated three times for a total of 18 plots. We hypothesized that crop height and an index of plant health: the normalized difference vegetation index (NDVI), would significantly decrease and that the sorghum's belowground biomass (BGB) would increase, as an indication of drought tolerance, in response to deficit irrigation. For both the 2021 and 2022 growing seasons, we measured changes in plant height, NDVI, and below-ground root response using a Leica C10 TLS, a MicaSense Altum multispectral camera mounted on a DJI Matrice 600 Pro sUAS, and an IDS GeoRadar RIS MF Hi-Mod dual frequency (400/900 MHz) GPR, respectively. Our hypotheses of a decrease in above-ground plant

traits, i.e., height for both varieties in response to deficit irrigation treatments were

confirmed. However, for NDVI, the red variety increased with decreasing water

availability, and the white variety was consistent with our hypothesis. We found

significant differences in the amplitude response maps, a surrogate of BGB phenology,

that indicated increasing biomass with increasing deficit irrigation. However, this

response was not consistent with field measures of BGB that showed the highest BGB at

60%, then 100%, and then 30%. This indicated that a 30% deficit level exceeded drought

tolerance for the two varieties. These results support the use of remote sensing

technologies for field plot-level plant health monitoring and crop phenotyping.

Acknowledgements

First, I'd like to thank my advisor Dr. Washington-Allen and my committee members Dr. Yerka and Dr. Louie for assisting me in designing and completing this intellectual work.

To my family and friends, thank you for your support and understanding throughout my graduate experience. In particular, I would like to thank my partner Ciara Sheets for supporting me throughout this degree.

To my fellow lab members and the community at UNR, thank you for being available to answer questions, and help with data analysis. Thank you to our undergraduate field assistant Ms. Kathryn McCray, you were a huge help to the data collection and processing work in 2022, and to Dr. Anuoluwapo Ogunleye for her help in data collection in 2021.

Table of Contents

Chapter 1: A literature review of multitemporal 3D crop phenotyping of above- and belowground traits using sUAS mounted multispectral camera, TLS, and GPR

Chapter 2: Towards 3D Crop Phenotyping of Above- and Belowground Grain Sorghum Plant Traits

Chapter 1

Multitemporal 3D Crop Phenotyping of Above- and Belowground Traits of Grain Sorghum using sUAS mounted multispectral camera, TLS, and GPR

Abstract: Increasing aridity due to climate change greatly alters soil stability and inhibits crop growth in the Southwestern United States. Sorghum [*Sorghum bicolor* L. Moench] is a key drought-tolerant species being used to replace less tolerant crops in drylands. Above- and below-ground crop productivity and the efficient use of water resources are critical aspects of sustainable agriculture, particularly in drylands. We will conduct a crop phenotyping study using three emerging remote sensing technologies to assess the response of above- and below-ground traits of two varieties of grain sorghum to deficit irrigation, i.e., drought conditions. In this chapter, I will provide an introduction and background on 1) the need for deficit irrigation in response to dwindling water supplies and increased aridity, 2) drought-tolerant sorghum, its origins, use, and establishment in the western US, 3) crop phenotyping through remote sensing, and 3) the three emerging remote sensing technologies to be used in this study including terrestrial laser scanning (TLS) to non-destructively measure 3-D changes in plant height, ground penetrating radar (GPR) to measure changes in root zone 3-D structure, and an airborne drone mounted multi-spectral camera that is used to measure changes in plant health. The goal of our study is to measure changes in plant traits that are indicative of drought tolerances in response to deficit irrigation. We hypothesized that aboveground traits such as height and plant health would decline in response to drought and that belowground traits such as root production would increase in response to drought, an indication of drought tolerance. We anticipate that our results will demonstrate the promise and efficacy of these three technologies for use in hi-throughput crop phenotyping in agriculture and that selectively bred sorghum varieties are a viable alternative for future use in dryland agriculture.

Keywords: Agriculture, Remote Sensing

1. Introduction

Approximately 98% of the land area in Nevada is estimated to be drylands [1]. Drylands are terrestrial land areas for which water limitations are defined by the aridity index (AI) as ≤ 0.65. The AI is calculated as the ratio of mean annual precipitation to mean annual potential evapotranspiration [2-5]. Globally and within Nevada, Drylands have been shown to have an increasing trend in temperature, aridity, and areal extent [6,7] a combination of which has greatly limited water availability and thus arable land for crop agriculture.

Sorghum [*Sorghum bicolor* L. Moench] is a drought-tolerant crop that originates in semiarid to arid North Africa and is the fifth most grown grain crop worldwide, with the US being the top producer [8]. Producers in Nevada report high local demand for food-grade sorghum for products like gluten-free food, snacks, and domestic craft brewing and distilling. Water management for this crop will be critical. Current water rights in Nevada mandate that newer farmers are the first to be shut off from irrigation once a minimum threshold is reached following a petition by producers in Eureka, Nevada[9]. Due to this, the development of drought-tolerant breeds of sorghum for Southwestern growers could play a key role in improving agriculture in climate-stricken regions. It is critically important for the stability and resilience of Nevada agriculture that producers have access to diverse, water-saving options. These efforts fulfill the land grant mission of the University of Nevada-Reno (UNR) and will help sustain grain sorghum production as it sees further growth. Consequently, the primary goal of this thesis is to compare the drought tolerance of two different varieties of grain sorghum under deficit drip irrigation using remote sensing technologies to measure the phenotypic response of above- and belowground characteristics including plant health, three-dimensional (3-D) structural phenology, and biomass.

2. Crop Phenotyping & Remote Sensing Technologies

2.1. TLS

TLS or terrestrial laser scanning is a form of ground-based light-detection-and-ranging (LIDAR). Lidar is an active sensor system that uses a laser at visible to infrared wavelengths to survey the x, y, and range (z) location of objects at adjustable resolutions, i.e., the spacing between scans as low as 0.5-mm, at frequencies ranging from 55,000 points per second (pts s^{-1}, e.g., Leica C-10 systems) to nearly 1 million pts s^{-1} depending on which TLS system is being used. TLS are survey-grade instruments with a ranging accuracy of ± 2 mm. For, time-of-flight instruments, distance (d) is determined from the detected range by measuring the elapsed round-trip time of flight (t) of a laser pulse incident on a survey point to the sensor:

$$d = ct / 2 \tag{1}$$

where c is the speed of light. Based on the distance and measures of the polar angles: azimuth and zenith the x, y, and z location can be calculated for each point and the resulting cluster of x, y, and z points is called a point cloud from which an array of 3-D crop structural parameters can be directly and indirectly derived including height, density, seed or fruit density, cover, yield, and biomass [10-13]. For example, Delgado [13] showed that herbicide-resistant monocot volunteers (wheat) could be mapped and separated from the dicot crop (canola) using the crop's height, green reflectance intensity value (GRI), and the GRI edge effect using a 532-nm wavelength TLS [14]. Eitel et al. [15,16] demonstrated that a 532-nm TLS can be used to detect chlorophyll a and b, xanthophyll, and the percent nitrogen content of agricultural crops. TLS systems at the 1550-nm wavelength are in the water absorption windows and have been used to measure leaf water content and this capability suggests that soil moisture could also be detected by this technology [17]. Further advances in structure-detecting models show promise for automated individual plant and plant parts, e.g., stems, leaves, and panicles, segmentation [18].

2.2. GPR

Ground penetrating radar or GPR is a non-destructive field instrument that actively transmits electromagnetic radar pulses into the ground to detect the reflected signals from belowground objects, including coarse roots (> 2-mm diameter [19]). Root traits that can be quantified using GPR include root depth, density, area, volume, biomass, and productivity [19-22]. For example, Butnor et al. (2001) were the first to map and estimate below-ground biomass of lateral roots in tree plantations using GPR, where they found a significant relationship (r = 0.55, p = 0.0274) between GPR amplitude reflectance and root biomass, thus laying the groundwork for estimation of belowground biomass and productivity using GPR in agricultural systems. Most recently, Zhou et al. (2022) [23]demonstrated the use of GPR to measure below-ground carbon stocks in savanna systems subject to different fire regimes. Guo et al. (2013), Liu et al. (2016), Atkinson et al. (2019), and Yang et al. (2020) [19,24-26] have reviewed the use of GPR in agriculture, particularly for crop phenotyping. Delgado et al. (2017, 2019) [22,27] were the first to use GPR to estimate below-ground biomass and net primary productivity of a tuber crop, i.e., the bulking rate or the accumulation of biomass overtime of cassava (*Manihot esculenta* C.). Additionally, GPR can be used to quantify volumetric soil moisture content from the relative dielectric permittivity [28,29]. Of particular interest to this study, Rodríguez-Robles et al. (2017) [30] were the first to use GPR and electrical resistivity tomography (ERT) to track below-ground water use in two competing dryland tree species.

2.3. sUAS

Small unoccupied aerial systems (sUAS) are capable of carrying payloads of various passive and active sensors that have been used in numerous agricultural studies including for crop phenotyping [26]. Multispectral sensor payloads can produce wide-ranging plant phenotyping metrics over a broad area. The use of structure-from-motion (SfM) provides the ability to create a 3-D representation of objects within a study site without the need for more expensive Lidar sensors [31]. Plant phenotyping structural metrics such as canopy cover, density, height, and volume can be derived from these 3-D products [32].

The use of multispectral imaging can provide plant health metrics such as the normalized difference vegetation index (NDVI) [33] or the soil adjusted vegetation index (SAVI) [34] as well as water use metrics including measures of evapotranspiration from thermal sensors [35] The combination of these metrics can be used to determine overall plant health and the effects of biotic and abiotic stress levels [32].

3. Discussion

We conclude that the collection of phenotypic traits via remote sensing is not only possible but can be highly efficient. These systems have the capability to produce a complete 3-D above and belowground phenotypic assessment of vegetation (Table 1). The application of terrestrial laser scanning (TLS) in an agricultural environment can produce a variety of plant health metrics such as height, cover, yield, biomass, Nitrogen content, chlorophyll content, and even leaf water content (Table 1). Lidar's versatility in deriving these metrics is limited by the wavelength of the laser and the user's available options in processing. As technological advances continue with new models, the application of TLS in the field can only become faster and easier. Further accessibility in airborne and UAV lidar will also greatly broaden the capabilities of the base technology. The use of ground penetrating radar (GPR) in agriculture is still in its infancy. Numerous studies have shown possible applications in coarse root biomass estimation as well as root phenotyping and estimating net primary productivity. Active application of GPR in an agricultural setting is still largely limited to research purposes due to the allowances needed for data collection e.g., wide row spacing and coarse root detection capabilities. However, ongoing advances in collection methodologies and the advance of airborne mounted GPR units show great promise for increasing the collection capabilities of this technology. Further work is being

Table 1. Three remote sensing technologies and their related metrics that may be used for crop phenotyping.

Technology	Metric	Advantages	Limitations	References
TLS	Height, 3D volume, Biomass, Green Intensity	High resolution 3D structure, millimeter level accuracy is possible	Prohibitive cost, Small landscape data collection, Large time investment	Hosoi and Omasa 2009 Leftsky et al 2009 Eitel et al 2014 Li et al 20148
GPR	Reflectance, root depth, cavernous space, water content	Non-destructive belowground metrics, high resolution product	Small landscape data collection, small body of literature	Butnor et al 2001 Delgado et al 2017 Klotzsche et al 2018
sUAS Multispectral Imagery	Height, 3D volume, Simple ration, NDVI, Evapotranspiration	Broad ranging sensor capabilities, landscape scale data collection,	No sub canopy information gathered, Issues with airspace usability, sunlight/shadows impact	Hassan et al 2019 Senay et al. 2010

undertaken expanding GPR data into fine scale root systems for a broader agricultural

application.

3.1. Thesis Goal and Predictions

The goal of this study is to use these three remote sensing technologies for crop phenotyping to

detect significant differences in crop traits in response to deficit irrigation, and thus drought stress. Crop

producers through the cooperative extension will be able to see firsthand how the use of high-efficiency,

drought-tolerant sorghum can be used to produce high-yield crops with low water use. In this study, the

above-and belowground phenotypic traits of grain sorghum in response to deficit irrigation will be

quantified using a multi-tiered remote sensing approach that includes three emerging technologies: time-

of-flight terrestrial laser scanning (TLS), dual-channel polarized ground penetrating radar (GPR), and a multispectral imaging payload on a UAV. UAV.

We hypothesized that aboveground traits such as height and plant health would decline in response to drought and that belowground traits such as root production would increase in response to drought, an indication of drought tolerance.

These technologies will allow us to evaluate above- and below-ground 3-D structural phenology and productivity of an agricultural crop in response to deficit irrigation. In Nevada, irrigation water comes primarily from groundwater sources that recent research via the GRACE satellite has indicated are in decline [36]. Groundwater availability is quite limited in Nevada with cutoffs in place to provide irrigation water for newer farmers. These combined effects put increased pressure on newer farmers to reduce water use as much as possible while still staying profitable.

References

1.   Robinson, N.P.; Allred, B.W.; Naugle, D.E.; Jones, M.O. Patterns of rangeland productivity and land ownership: Implications for conservation and management. *Ecological applications : a publication of the Ecological Society of America.* **2019**, *29*, doi:10.1002/eap.1862.

2.   Grove, A.T. WORLD ATLAS OF DESERTIFICATION, 2nd edition, edited by N. J. Middleton and D. S. G. Thomas, Arnold, London, 1997. No. of pages: x + 182. Price: £145.00 (hb). ISBN 0-340-69166-2. *Earth Surface Processes and Landforms* **1999**, *24*, 280-280, doi:https://doi.org/10.1002/(SICI)1096-9837(199903)24:3<280::AID-ESP955>3.0.CO;2-7.

3.   Safriel, U.; Adeel, Z. Development paths of drylands: thresholds and sustainability. *Sustainability Science* **2008**, *3*, 117-123.

4.   Zomer, R.J.; Trabucco, A.; Bossio, D.A.; Verchot, L.V. Climate change mitigation: A spatial analysis of global land suitability for clean development mechanism afforestation and reforestation. *Agriculture, ecosystems & environment* **2008**, *126*, 67-80.

5.   Zomer, R.J.; Xu, J.; Trabucco, A. Version 3 of the global aridity index and potential evapotranspiration database. *Scientific Data* **2022**, *9*, 409.

6.   Huang, J. Accelerated dryland expansion under climate change. Yu, H., Ed. 2016.

7.   Delgado-Baquerizo, M.; Soliveres, S.; Hernández-Clemente, R.; Zhao, Y.; Gaitán, J.J.; Berdugo, M.; Delgado-Baquerizo, M.; Soliveres, S.; Hernández-Clemente, R.; Zhao, Y., et al. Global ecosystem thresholds driven by aridity. *Science.* **2020**, *367*, 787-790, doi:10.1126/science.aay5958.

8.   Mundia, C.W.; Secchi, S.; Akamani, K.; Wang, G. A regional comparison of factors affecting global sorghum production: The case of North America, Asia and Africa's Sahel. *Sustainability* **2019**, *11*, 2135.

9.   King, J. State-Engineer-Order-No.-1302-Diamond-Valley-Hydrographic-Basin-07-153-Eureka-County-Nevada. Nevada, O.O.T.S.E.O.T.S.O., Ed. Office of Nevada State Engineer: Carson City, 2019.

10.   Hosoi, F.; Omasa, K. Estimating vertical plant area density profile and growth parameters of a wheat canopy at different growth stages using three-dimensional portable lidar imaging. *ISPRS Journal of Photogrammetry and Remote Sensing* **2009**, *64*, 151-158.

11.   Hosoi, F.; Omasa, K. Estimation of vertical plant area density profiles in a rice canopy at different growth stages by high-resolution portable scanning lidar with a lightweight mirror. *ISPRS journal of photogrammetry and remote sensing* **2012**, *74*, 11-19.

12.   Ehlert, D.; Adamek, R.; Horn, H.-J. Laser rangefinder-based measuring of crop biomass under field conditions. *Precision Agriculture* **2009**, *10*, 395-408.

13.   Long, D.S.; McCallum, J.D. Mapping straw yield using on-combine light detection and ranging (lidar). *International journal of remote sensing* **2013**, *34*, 6121-6134.

14.   Delgado, A. Southern Great Plains Expansion of Glyphosate Resistant Brassica Napus L.: Management and Mapping. 2013.

15.   Eitel, J.U.; Vierling, L.A.; Long, D.S. Simultaneous measurements of plant structure and chlorophyll content in broadleaf saplings with a terrestrial laser scanner. *Remote sensing of Environment* **2010**, *114*, 2229-2237.

16.   Eitel, J.U.; Magney, T.S.; Vierling, L.A.; Brown, T.T.; Huggins, D.R. LiDAR based biomass and crop nitrogen estimates for rapid, non-destructive assessment of wheat nitrogen status. *Field Crops Research* **2014**, *159*, 21-32.

17.   Junttila, O.S.; Vastaranta, M.A.; Linnakoski, R.M.; Sugano, J.; Kaartinen, H.; Kukko, A.; Holopainen, M.E.; Hyyppä, H.; Hyyppä, J. Measuring leaf water content using multispectral

terrestrial laser scanning. *International Archives of the Photogrammetry, Remote Sensing & Spatial Information Sciences* **2017**.

18. Guo, Q.; Su, Y.; Hu, T.; Guan, H.; Jin, S.; Zhang, J.; Zhao, X.; Xu, K.; Wei, D.; Kelly, M. Lidar boosts 3D ecological observations and modelings: A review and perspective. *IEEE Geoscience and Remote Sensing Magazine* **2020**, *9*, 232-257.

19. Guo, L.; Chen, J.; Cui, X.; Fan, B.; Lin, H. Application of ground penetrating radar for coarse root detection and quantification: a review. *Plant and soil* **2013**, *362*, 1-23.

20. Hruska, J.; Cermak, J.; Sustek, S. Mapping tree root systems with ground-penetrating radar. *Tree physiology.* **1999**, *19*, 125-130, doi:10.1093/treephys/19.2.125.

21. Butnor, J.R.; Doolittle, J.; Kress, L.; Cohen, S.; Johnsen, K.H. Use of ground-penetrating radar to study tree roots in the southeastern United States. *Tree physiology* **2001**, *21*, 1269-1278.

22. Delgado, A.; Hays, D.B.; Bruton, R.K.; Ceballos, H.; Novo, A.; Boi, E.; Selvaraj, M.G. Ground penetrating radar: a case study for estimating root bulking rate in cassava (Manihot esculenta Crantz). *Plant methods* **2017**, *13*, 1-11.

23. Zhou, Y.; Singh, J.; Butnor, J.R.; Coetsee, C.; Boucher, P.B.; Case, M.F.; Hockridge, E.G.; Davies, A.B.; Staver, A.C. Limited increases in savanna carbon stocks over decades of fire suppression. *Nature* **2022**, *603*, 445-449.

24. Liu, X.; Dong, X.; Leskovar, D.I. Ground penetrating radar for underground sensing in agriculture: a review. *International Agrophysics* **2016**, *30*.

25. Atkinson, J.A.; Pound, M.P.; Bennett, M.J.; Wells, D.M. Uncovering the hidden half of plants using new advances in root phenotyping. *Current opinion in biotechnology* **2019**, *55*, 1-8.

26. Yang, W.; Feng, H.; Zhang, X.; Zhang, J.; Doonan, J.H.; Batchelor, W.D.; Xiong, L.; Yan, J. Crop phenomics and high-throughput phenotyping: past decades, current challenges, and future perspectives. *Molecular Plant* **2020**, *13*, 187-214.

27. Delgado, A.; Novo, A.; Hays, D.B. Data acquisition methodologies utilizing ground penetrating radar for cassava (Manihot esculenta Crantz) root architecture. *Geosciences* **2019**, *9*, 171.

28. Huisman, J.A.; Hubbard, S.S.; Redman, J.D.; Annan, A.P. Measuring soil water content with ground penetrating radar: A review. *Vadose zone journal* **2003**, *2*, 476-491.

29. Klotzsche, A.; Jonard, F.; Looms, M.C.; van der Kruk, J.; Huisman, J.A. Measuring soil water content with ground penetrating radar: A decade of progress. *Vadose Zone Journal* **2018**, *17*, 1-9.

30. Rodríguez-Robles, U.; Arredondo, T.; Huber-Sannwald, E.; Ramos-Leal, J.A.; Yépez, E.A. Application of geophysical tools for tree root studies in forest ecosystems in complex soils. *Biogeosciences* **2017**, *14*, 5343-5357.

31. Hassan, M.A.; Yang, M.; Fu, L.; Rasheed, A.; Zheng, B.; Xia, X.; Xiao, Y.; He, Z. Accuracy assessment of plant height using an unmanned aerial vehicle for quantitative genomic analysis in bread wheat. *Plant Methods* **2019**, *15*, 1-12.

32. Li, L.; Zhang, Q.; Huang, D. A review of imaging techniques for plant phenotyping. *Sensors* **2014**, *14*, 20078-20111.

33. Rouse, J.W.; Haas, R.H.; Schell, J.A.; Deering, D.W. Monitoring vegetation systems in the Great Plains with ERTS. *NASA Spec. Publ* **1974**, *351*, 309.

34. Huete, A.R. A soil-adjusted vegetation index (SAVI). *Remote sensing of environment* **1988**, *25*, 295-309.

35. Savoca, M.E.; Senay, G.B.; Maupin, M.A.; Kenny, J.F.; Perry, C.A. *Actual evapotranspiration modeling using the operational Simplified Surface Energy Balance (SSEBop) approach*; US Department of the Interior, US Geological Survey: 2013.

36. Famiglietti, J.S. The global groundwater crisis. *Nature Climate Change* **2014**, *4*, 945-948.

Chapter 2

Article

Towards 3D Crop Phenotyping of Above- and Belowground Grain Sorghum Plant Traits

Russell S. Godkin[1], Robert A. Washington-Allen[1*], Melinda K. Yerka[1], Manuel Andrade-Rodriguez[1], Erin L. Smith[1], Uriel Cholula Rivera [1], Alfredo Delgado[2], Maninder K. Walia[3], Kathryn McCray[1], and G. McCuin[3]

[1] Department of Agriculture, Veterinary & Rangeland Science, University of Nevada, Reno, Reno, NV, rgodkin@unr.edu, rwashingtonallen@unr.edu, yerka@unr.edu, andrade-rodriguez@unr.edu. esmith@gmail.com, cholulua-rivera@unr.edu, kmccray@nevada.unr.edu

[2] Agricultural Geosystems Department, IDS GeoRadar, North America, Golden, CO, adelgado@idsgeoradar.com

[3] University of Nevada Cooperative Extension (UNCE), College of Agriculture, Biotechnology & Natural Resources, University of Nevada, Reno, Reno, NV

* Correspondence: rgodkin@unr.edu

Abstract: Increasing aridity due to climate change is altering soil stability and inhibiting crop growth in the Southwestern United States. Sorghum [*Sorghum bicolor* L. Moench] is a key drought-tolerant species being used to replace less drought-tolerant crops in drylands. Above- and below-ground crop productivity and the efficient use of water resources are critical aspects of sustainable agriculture, particularly in drylands. We conducted a crop phenotyping study using three emerging remote sensing technologies to assess the response of above- and below-ground traits of two varieties of grain sorghum

to deficit irrigation, i.e., drought conditions. We hypothesized that crop height and an index of plant health: the normalized difference vegetation index (NDVI), would significantly decrease and that the sorghum's belowground biomass (BGB) would increase, as an indication of drought tolerance, in response to deficit irrigation. We used a randomized block design, with three levels of deficit irrigation treatment (100, 60, and 30% of replenishment of soil water depletion to field capacity) as the main plots, two hybrids of grain sorghum as the subplot, and three replications. Over the course of the 2021 and 2022 growing seasons, we measured changes in plant height, NDVI, and below-ground root response using a 532-nm terrestrial laser scanner (TLS), a multispectral camera mounted on an airborne drone, and a 900 MHz ground penetrating radar, respectively. Our hypotheses of a decrease in above-ground plant traits, i.e., height for both varieties and NDVI in the white variety in response to deficit irrigation treatments were confirmed. We found significant differences in the amplitude response maps, a surrogate of BGB phenology, that indicated increasing biomass with increasing deficit irrigation. However, this response was not consistent with field measures of BGB that showed the highest BGB at 60%, then 100%, and then 30%. This indicated that a 30% deficit level exceeded drought tolerance for the two varieties. These results demonstrated that these three technologies have great promise for use in hi-throughput crop phenotyping in agriculture and that selectively bred sorghum varieties are a viable alternative for future use in dryland agriculture.

Keywords: Agriculture, Remote Sensing

1. Introduction

Over 40% of the Earth's ice-free land area is composed of drylands that act as vital carbon sinks [1] and comprise around 31% of the total land area in the United States [2]. Within Nevada, 98% of the land is defined as drylands with an aridity index (AI) ≤ 0.65, and some of these landscapes contain arable soils that are available for agriculture [3-6]. These drylands have seen an increase in temperature and aridity threatening the already limited arable landscape [7,8]. Dryland agriculture comprises a major component of Nevada's economy with alfalfa and wheat being the two primary crops [9]. Globally, increasing temperatures, drought, and aridity are greatly affecting agriculture within drylands including Nevada [7,8,10]. In Nevada, irrigation water comes primarily from groundwater sources that recent research via the gravity recovery and climate experiment (GRACE) satellite has indicated are currently in decline [11]. Groundwater availability is quite limited in Nevada with cutoffs in place to reduce water use starting with newer farmers[12]. These combined effects put increased pressure on newer farmers to reduce water use as much as possible while still staying profitable.

These issues combined with ongoing water rights create a difficult environment for new farmers in Nevada. Unfavorable conditions provide an incentive to select for by crop breeding and plant drought-tolerant alternative crops such as sorghum. Sorghum is the fifth highest-produced grain crop in the world with a diverse genetic pool suitable for creating different breed varieties tolerant to heat and drought [13,14]. The development of efficient phenotyping techniques for these new varieties of sorghum is critically important. Small unoccupied aircraft systems (sUAS) have become readily available to consumers and are in steady use by producers for simple mapping tasks and monitoring. Larger corporations have the ability to utilize these devices to a greater extent, but a number of applications have yet to be fully adopted. Simple orthomosaics of fields using red, green, blue (RGB) cameras are good for continuous monitoring of visible spectral phenotypes, but other specialized metrics such as vegetation

health indices and above-ground water use can be difficult to apply due to a lack of introductory resources. The rapidly developing world of lidar (light detection-and-ranging) offers even greater avenues for 3-D plant structural phenotyping as well as spectral-based metrics for the detection of nitrogen levels, chlorophyll content, or even leaf water content [15-17]. The implementation of structure-detecting models allows for automated plant segmentation and the identification of separate plant organs such as leaves, stems, and panicles [18]. The unique capabilities of ground penetrating radar (GPR) in agriculture offer the possibility of non-invasive belowground biomass detection and root phenotyping [19-21]. Unique to this study will be the simultaneous application of 2 active and 1 passive remote sensing technology to crop phenotyping of above- and below-ground plant traits including the use of terrestrial laser scanning (TLS), GPR, and a small unoccupied aerial system (sUAS) with a multispectral imaging camera payload.

Consequently, in this study, the above-and belowground phenotypic traits of grain sorghum in response to deficit irrigation will be quantified using a multi-tiered remote sensing approach that includes three emerging technologies: time-of-flight TLS, dual-channel polarized GPR, and a multispectral imaging camera payload that is mounted on an sUAS. These technologies will allow us to evaluate above- and below-ground 3-D structural phenology and productivity of an agricultural crop in response to deficit irrigation.

1.1 Goal and Hypotheses

The goal of this study is to use 3 remote sensing technologies for crop phenotyping to detect significant differences in crop traits in response to three levels of deficit irrigation (30%, 60%, 100%), and thus drought stress. We hypothesized that the remotely-sensed aboveground metrics, including crop height and a plant health metric, would exhibit a decline and that belowground metrics, including root

structure and/or biomass, would exhibit an increase in response to drought, i.e., deficit irrigation, indicating evidence of drought tolerance.

2. Materials and Methods

2.1. Study Site

The experimental plots were established in 2021 and 2022 at the 11-ha University of Nevada's College of Agriculture, Biotechnology & Natural Resources Valley Road Field Laboratory (UNR CABNR-VRFL) in Reno, Nevada (Figure 1). Weather data for the study site was collected from an onsite weather station [22]. Mean high temperatures for the growing season (June – October) range from 20- 27°C with lows ranging from 4-14°C. Mean precipitation is low ranging between 0-20 mm. The VRFL's soils are an Orr gravelly loam and Orr sandy loam (Fine-loamy mixed, superactive, mesic Aridic Argixerolls,)[23]. Field data was collected starting directly before planting and continued until harvest (approximately early June to the first week of October).
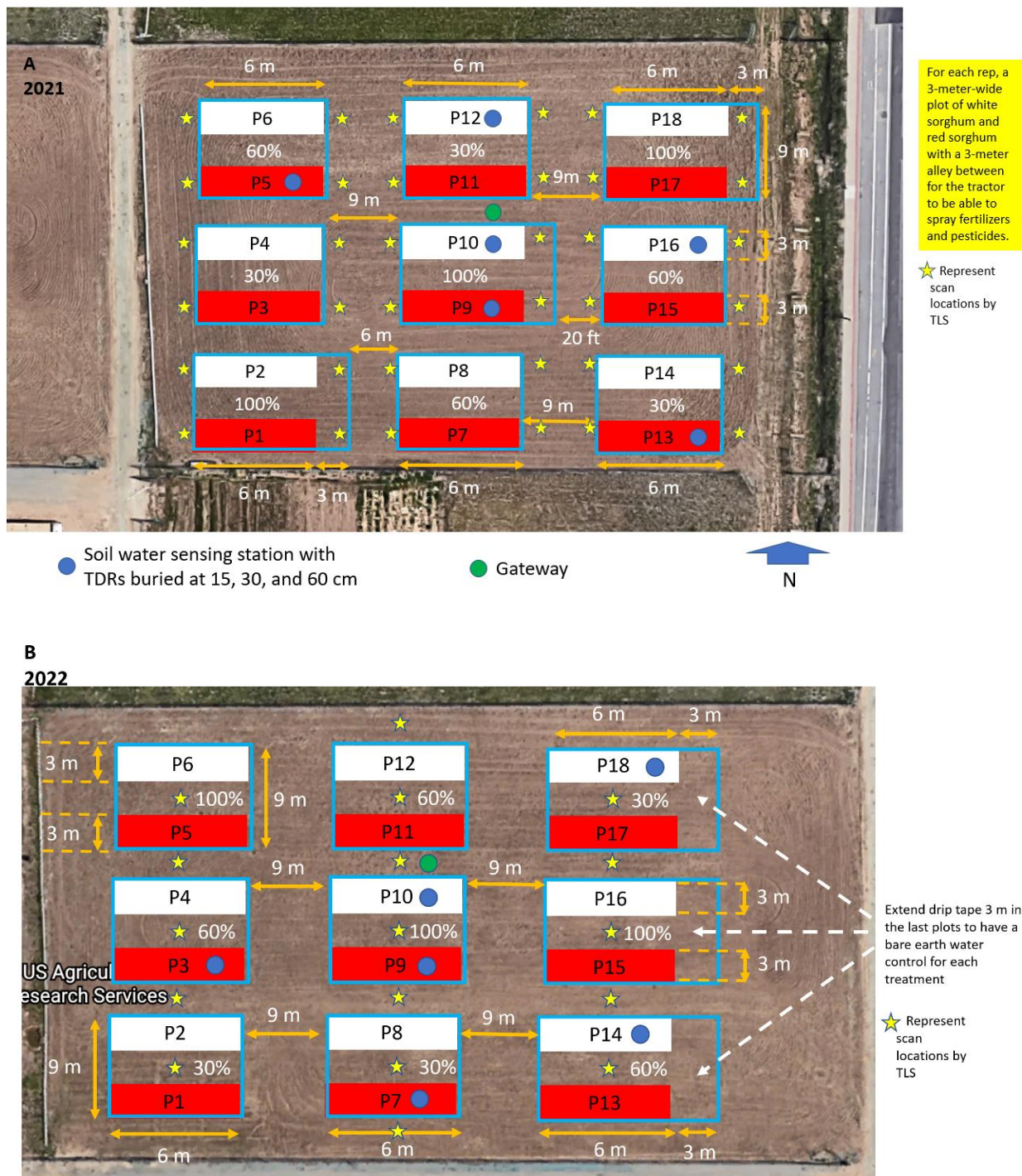
Figure 1. The experimental plot designs for the remote sensing crop phenotyping study that was conducted in 2021 (A) and 2022 (B) at the University of Nevada CABNR Valley Road Field Laboratory in Reno, Nevada. A randomized block design was used with 3 levels of deficit irrigation treatments X 2 hybrid varieties of grain sorghum X 3 replications for 18 total 6 m X 3 m field plots. TLS = Terrestrial Laser Scanner and TDR = Time Domain Reflectance.

2.2 2021 and 2022 Field Experimental Design

In June of 2021, two varieties of sorghum (Richardson Seeds Early Red Hybrid and Early White Hybrid) were planted. We used a randomized block design, with three levels of deficit irrigation treatments (100, 60, and 30% of replenishment of soil water depletion to field capacity) as the main plots, two hybrids of grain sorghum as the subplot, and three replications. A total of 18 6-m X 3-m plots were generated by this experimental design. A single 6-m X 3-m plot contains 4 X 6 m rows with 76 cm (30 in) spacing between rows each of which was sowed to one of the varieties of sorghum at 15-cm spacing. This may produce an estimated 40 plants per row and a total of 160 plants per plot. The row spacing of 76 cm was set to allow ground penetrating radar (GPR) collections for each plot of sorghum. Total water use (100%) was determined with time domain reflectometry (TDR) for establishing a deficit irrigation system. Three sets of drip irrigation treatments (100%, 60%, 30%) were established for each sorghum variety creating six plots which were then replicated three times (Figure 1 A and B).

In mid-July of 2022 when the sorghum panicle had reached the grain-filling stage of growth, wild bird depredation began to occur primarily from Mourning doves (*Zenaida macroura*) and what appeared to be starlings. In response to these granivores, we placed bird netting over all 18 plots in early August 2022, which had to be removed weekly for remote sensing data collection.

2.3. TLS Plant Height Measurements & Processing

The TLS survey period for the 2021 season began on 6/30/21 and ran until the first week of October (10/05/21). The 2022 field season took place from 6/08/22 until 10/12/22. These time frames captured the entire growth cycle of both sorghum varieties. Terrestrial laser scanning (TLS) was conducted using a Leica C10 532 nm green laser capable of up to 50,000 points/sec that emits a time of

flight-based laser for distance calculations. A full list of TLS specifications can be found in Table 1. A

preliminary scan was taken shortly after planting to act as a reference for a bare earth scan for the

generation of a raster canopy height model (CHM) of a field plot. Subsequent scans were taken weekly

following crop emergence with a total of 9 usable dates collected during the 2021 growing season and 12

during the 2022 season. In each instance of data collection, a minimum of 15 scan positions were taken at

a height of 2 meters above the ground to capture all plots thoroughly and to minimize obstructions.

Reflective sphere targets were placed across the field in positions that were visible from all scan locations

in order to assist with scan-to-scan registration. The scan positions for the 2021 and 2022 field seasons are

shown in Figure 1.

The overall workflow for TLS processing is shown in Figure 2. TLS postprocessing consisted of

(1) registration of all scans and point-to-point merging, (2) the clipping out of extraneous points and stray

point filtering, (3) conversion to raster and extraction of regions of interest (ROI), and (4) statistical

analysis of derived metrics. Scan registration was performed using Leica Register 360™ automatic

registration. Here, corresponding tie points are identified by the algorithm and theoretical scan positions

are displayed for manual approval. Any scan positions that can't be automatically placed are then

manually positioned using the visual alignment tool in Leica Register 360 before automatic registration is

performed again.

The merged point clouds still contain noise and excess data caused by dust particles and regions

outside the experimental zone. All point clouds were reduced down to only the study site using the

software CloudCompare's segment tool to remove the majority of stray points and reduce file size [24].

Further filtering was performed using the Point Data Abstraction Library's (PDAL) filters.outlier function

[25]. Point clouds were then gridded into 5 cm raster files using PDAL's inverse distance weighted (IDW)

writers.gdal function [26] to create digital surface models for canopy height model (CHM) generation.

CHM's are generated using a gridded bare earth scan functioning as a digital terrain model (DTM) and georegistered to digital surface models (DSM) from the TLS data. Raster subtraction of the DSM minus the DTM was conducted using QGIS software raster calculator [27]. The resulting CHM contains only height data. A ROI vector coverage was digitized of the experimental plots (Figure 1) and used for data extraction. Each of the weekly 18 X 5 cm pixel resolution rasters of a field plot was then analyzed in a time series by plotting the mean height values over time. A one-way analysis of variance was performed after increasing the raster resolution to 20 cm to reduce file size and spatial autocorrelation. A Tukey's post hoc test was then performed to detect differences between treatment plots.

Registration
↓
Crop and Filter
↓
Grid to Raster
↓
Extract ROIs
↓
Statistical Analysis
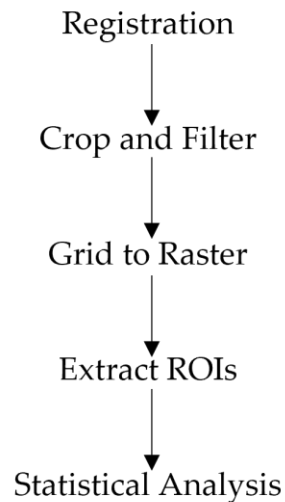
Figure 2. TLS post-processing workflow for CHM generation and analysis of the UNR-CABNR Valley Rd Laboratory sorghum plots in Reno, NV.

Table 1. Specification of TLS Leica C10 used in the study of the UNR-CABNR Valley Rd Laboratory sorghum plots in Reno, NV.

Characteristic	Description
Wavelength	Green, 532 nm visible
Range	300 m @ 90%; 134 m @ 18% albedo
Scan Rate	Up to 50,000 points/sec

Scan Resolution	At a range between 0 – 50 m: Spot Size: from 4.5 mm (FWHM-Based); 7 mm (Gaussian based)
	Point Spacing: Fully selectable horizontal and vertical; < 1 mm minimum spacing, through full range; single point dwell capacity
Field-of-View	Horizontal: 360° (maximum)
	Vertical: 270° (maximum)

2.4. GPR Data Collection, Depth Calibration, & Processing

In 2021, on 9 different occasions during the sorghum growing season, ground penetrating radar (GPR) amplitude reflectivity maps (scans) were made of the 18 field plots of grain sorghum (Figure 3). In 2022, on 10 different occasions during the growing season, GPR scans were collected. These collections were made using an IDS GeoRadar RIS MF Hi-Mod dual channel (400 /900 MHz) system with horizontal transmit and horizontal receiving polarization (HH) (Table 2). Only the 900 MHz amplitude returns were considered for the 2021 and 2022 experiments due to the small diameter and shallow rooting depth of the two varieties of grain sorghum. Previous research had established that higher frequency antennas produce higher resolution imaging on belowground structures compared to lower frequency antennas [20,28,29]. GPR data geolocation was established using two Emlid Reach RS2 (a base station and a rover) multi-band real-time kinematic (RTK) global positioning systems (GPS). The attachment of the rover GPS to the GPR cart absolved the need for wheel-measured transects commonly used in GPR data collection and allowed freedom of movement that is helpful to field application. GPR data acquisition was accomplished using IDS GeoRadar's OneVision™ collection software whereby the GPR was systematically rolled in a cart up down/up rows parallel to the plants forming a bidirectional grid (Figure

3). This was repeated across all plots and replicates on a weekly basis beginning in late May before planting and continuing from June to October of 2021 and 2022.

GPR post-processing was performed using GPR-Slice software [30] of which the data processing steps are shown in Figure 4. These steps are as follows: (1) digitize amplitude millivolts to 16-bit and apply a batch gain-wobble, (2) set the ground level to time 0 using the Scan-by-Scan method, (3) radar spectra hi/lo cut-off points are set as half above and below the 900 MHz frequency (450/1350 MHz) and an Automatic Gain Control (AGC) gain is applied, (4) apply a bandpass filter to the data followed by a Hilbert transformation, (5) the radargram of the amplitude returns was then XYZ-orientation sliced at 10 slices with 15% overlap, and these slices were then IDW gridded to 5 cm pixel resolution radar amplitude reflectance rasters for image analysis. Due to the shallow rooting depth of the sorghum roots for both varieties, only the first slice was used for analysis as that is where the bulk of the root mass was located. Raster analysis was performed using QGIS [27] open-source software for ROI extraction and time series analysis by plotting the mean amplitude reflectivity values over time. ROIs of each treatment plot were extracted and resampled to 20 cm pixel resolution before being converted into R data frames for analysis in the R statistical package [31]. Each GPR cart turnaround section of the data collection was removed from the data frame as these resulted in high-velocity returns as the GPR was partially lifted for the 180° turns. A one-way analysis of variance (ANOVA) and Tukey's post hoc test using R's stat module [31] were conducted on the split-plot experimental design using the GPR's amplitude reflectivity values as the response variable to 3 levels of deficit irrigation.
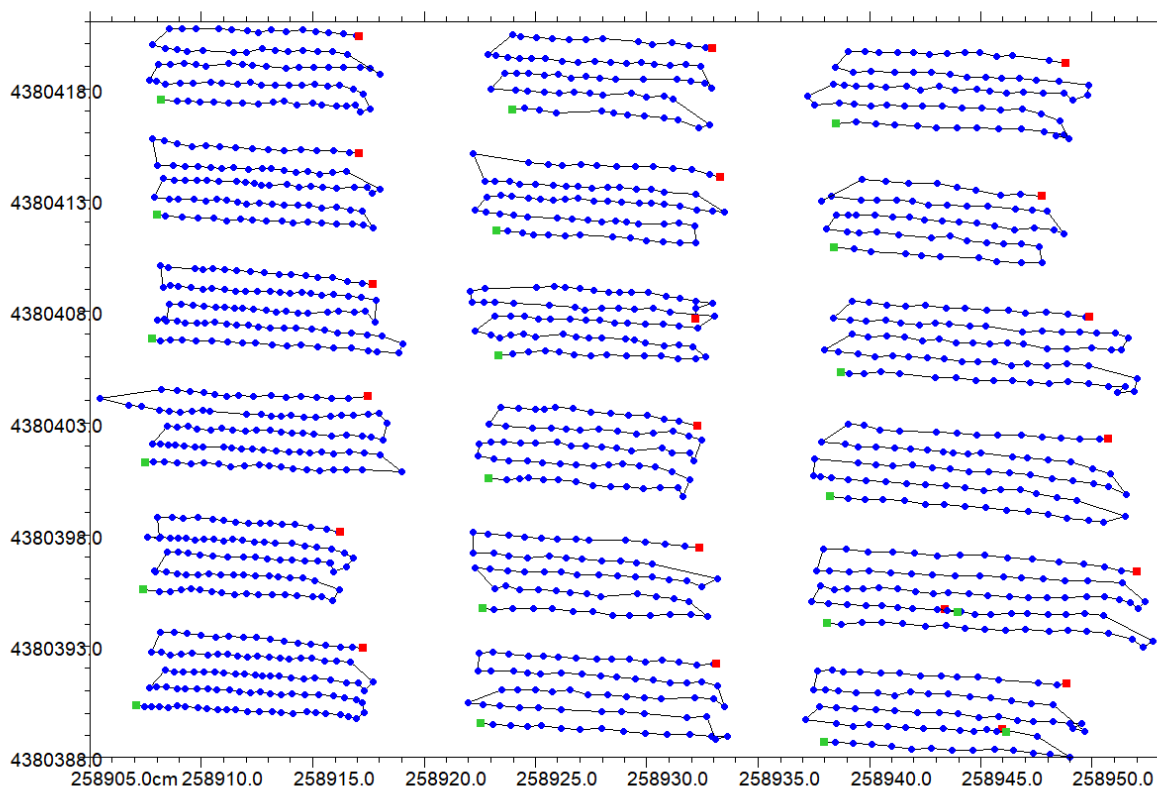
Figure 3. Example of the recorded GPS positions of the GPR during data acquisition of a surrogate of belowground biomass for eighteen plots of two varieties of grain sorghum in a systematic bidirectional grid pattern at the UNR CABNR Valley Road Laboratory, Reno, NV.

Radargram 16 bit – 16 bit + Batch
Gain - Wobble

↓

Time-zero correction

↓

Spectra hi/lo cut off + AGC gain

↓

Bandpass filtering+ Hilbert
transformation

↓

Slice XYZ

↓

IDW gridding
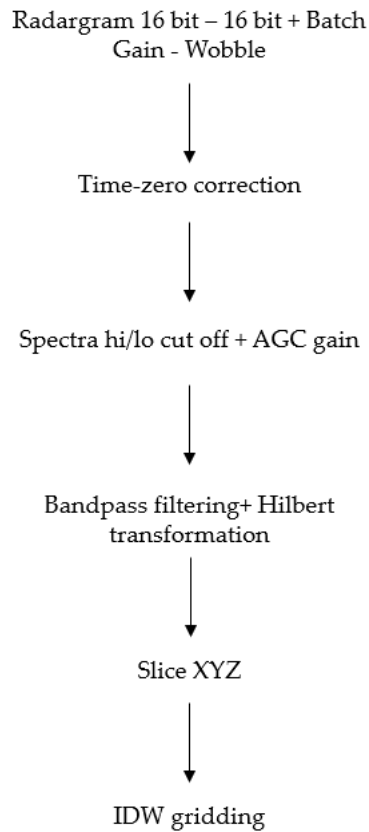
Figure 4. GPR-Slice step-by-step methods were used for the post-processing of GPR data for eighteen plots of two varieties of grain sorghum at the UNR CABNR Valley Road Laboratory, Reno, NV.

Table 2. The product specifications of an IDS GeoRadar RIS MF Hi-Mod dual frequency GPR used for detecting belowground 3D structure including biomass of eighteen plots of two varieties of grain sorghum at the UNR CABNR Valley Road Laboratory, Reno, NV.

Characteristic	Description
Footprint	38 x 43 cm (Single antenna)
Channels	2 (up to 8)
Frequency	400 MHz / 900 MHz
Polarization	Horizontal (HH)
Antenna Spacing	50 cm
Samples/scan	512

2.5. sUAS-Mounted Multispectral Camera NDVI Collection & Processing

Multispectral data of the 18 field plots were collected for the 2021 and 2022 field seasons using a MicaSense Altum 6 band (red, green, blue, red edge, near-infrared (NIR), and short wave infrared (SWIR)) camera that was mounted on an sUAS DJI Matrice 600. Four flights on four different occasions were collected in 2021 and 5 flights were conducted between early July to late September in 2022. Flight parameters for both field seasons can be found in Table 3 and camera specifications are provided in Table 4. Only 5 flights could be made in 2022 because of a lowering of the drone-accessible flight deck to zero elevation over the University by the local FAA. The allowed flights for both years were conducted using Pix4D Capture flight planning and processing software at a height of 15 meters above ground level at a slow speed (2 m/s). A 70% frontal and 60% side image overlap was used for the 2021 season and an 80% front and side for the 2022 season. The low altitude and slow flight speed were required to ensure proper overlap of images. Despite these measures, some flights from the 2021 field season failed to fully process due to camera errors. This problem was corrected for the 2022 season by slowing the camera capture rate and increasing flight plan overlap according to MicaSense's recommendations. Three ground control points were established across the field for each flight using Emlid RS2 RKT GPS rover and base units. Image processing was performed using Pix4D Mapper's agriculture settings to generate multispectral orthomosaics and the NDVI spectral index [32]. NDVI was calculated as:

$$NIR - R / NIR + R \qquad (2)$$

Spectral orthomosaics were output at 0.6 cm pixel resolution. Each plot was extracted using ROI's and mean NDVI values were plotted over time. The data was resampled to 20 cm pixel resolution and analyzed using a one-way ANOVA and Tukey's post hoc analysis to determine differences in treatments.

Table 3. sUAS flight parameters used for both the 2021 and 2022 field seasons for the remote sensing crop phenotyping study on eighteen plots of two varieties of grain sorghum at the UNR CABNR Valley Road Laboratory, Reno, NV.

Software	Altitude	Front/Side overlap	Resolution

Pix4D	15m	70/60%	0.6 cm
		85/85%	

Table 4. Specifications for the MicaSense Altum camera that was mounted on the airborne drone for this remote sensing crop phenotyping study on eighteen plots of two varieties of grain sorghum at the UNR CABNR Valley Road Laboratory, Reno, NV.

Parameters	Multispectral	Thermal
CCD Size	3.45 μm	12 μm
Resolution	2064 x 1544 px (3.2 MP x 5 imagers)	160 x 120 px (0.01 K)
Aspect ratio	4 : 3	4 : 3
Sensor size	7.12 x 5.33 mm (8.9 mm diagonal)	1.92 x 1.44 mm
Focal length	8 mm	1.77 mm
Field of view (h x v)	48° x 36.8°	57° x 44.3°
Thermal sensitivity	N/A	< 50 mK
Thermal accuracy	N/A	+/- 5 K
Output bit depth	12-bit	14-bit
GSD @ 120 m (~400 ft)	5.2 cm	81 cm
GSD @ 60 m (~200 ft)	2.6 cm	41 cm

2.6. Biomass Collections

When the 2022 crop was ready for harvest, in each of the 3 m X 6 m X 18 plots, a 0.5 m^2 sub-plot was established at the center of each plot for each sorghum variety and a sample of pannicles were collected to later estimate grain yield. Each of the full plots was mowed around these center plots and the mowed plants were simultaneously weighed by the mower's scale for above-ground wet biomass. After the mowing, the 0.5 m^2 sub-plots were then excavated using a backhoe to collect both above and below-ground biomass. The mowed sorghum plants from the subplot were then washed of all soil, partitioned into pannicles, stems, and roots, and weighed for wet above- and below-ground biomass, and dried at

49°C for 48 hours. The sub-plot's estimates of above-ground wet biomass were then added to the wet biomass of the corresponding full plot for an estimate of the total plot wet above-ground biomass. The wet-to-dry above- and below-ground biomass conversion factor was estimated. The 0.5 m² below-ground wet and dry biomass samples were then scaled to the individual 6 m rows X 4 rows/plot to estimate the total plot below-ground biomass/variety.

2.7. Random Forest Model and Linear Regression for biomass estimation

A Random Forest (RF) is a machine learning tool that is an ensemble of regression trees that are recursively generated to produce best-fit regression models [33]. An RF model that used the field plot spatial data was used in this study using the R statistical software's caret classification and regression package to try to predict the best-fit models for estimates of above-ground biomass in each of the sorghum fields in 2022. The variables used as predictors included the 2022 mean CHM, mean NDVI, and mean red-edge NDVI. The red edge NDVI was created using the R statistics program [31] and the equation (3) below:

$$\frac{RE - R}{RE + R} \tag{3}$$

The above-ground biomass response variable spatial layer was created by generating a 0.5-m X 0.25 m pixel resolution raster along the 18 field plot's 4 X 6 m rows and evenly distributing the estimated wet above-ground biomass values for the corresponding plot to these pixels.

3. Results

3.1. TLS 2021

Mean heights derived from the canopy height model show the phenological development of both varieties of sorghum over the course of the growing season (Figure 6). Mean height increased rapidly until late July before plateauing in height.
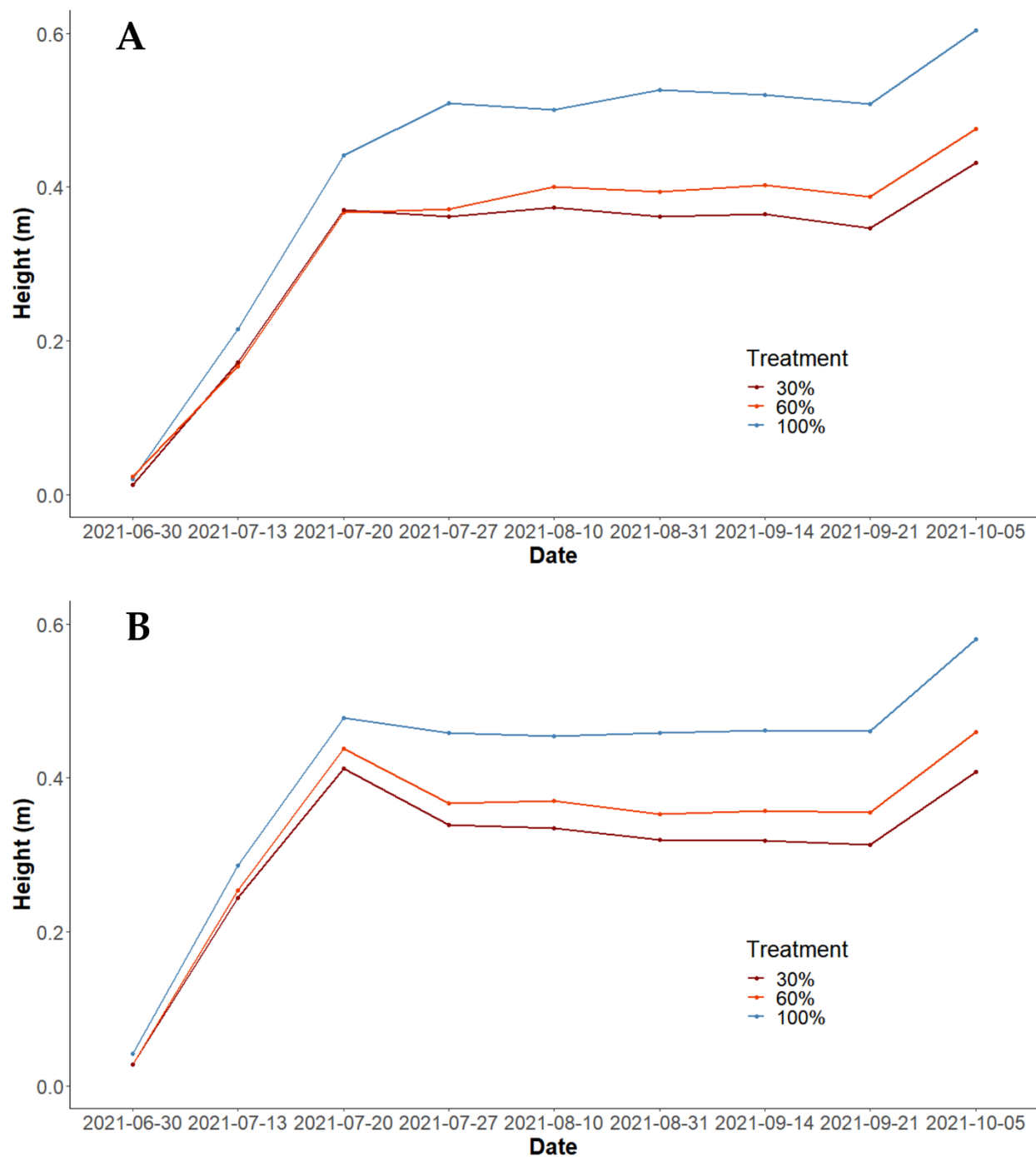
Figure 5. The 2021 TLS-generated mean canopy height model (CHM) for the white (A) and red (B) varieties of sorghum in response to 3-levels of deficit irrigation versus TLS collection dates indicate the phenology of the two varieties. This crop phenotyping study was conducted at the UNR CABNR Valley Road Laboratory, Reno, NV.

3.1.1 White

TLS analysis of variance (ANOVA) results showed significant differences in the first week of scans between each treatment, however plant heights at this time were between 10-15 cm tall, and differences in height are likely due to wind effects on the developing plants. A reliable significant difference (p-value of near zero for 100-60/30) in height between the 100% deficit irrigation when compared to the 60% level and 100% to the 30% began on the second week of scanning 7/13/2021, one month after planting. No significant difference in height between 60% and 30% was detected until 8/10/21. Beyond that point in the season, all three treatments showed significant differences in height (p-value < 0.05) as seen in Appendix A1.

3.1.2 Red

The TLS ANOVA results for the red variety showed a divergence in treatments earlier in the growing season than the white. Significant differences in heights were detected by the second week of data collection (7/13/2021) with p-values of 0, 0, 0.008 for the 100-60, 100-30, 60-30% irrigation, respectively (Appendix A2). Significant differences (p-value near 0) in height across all treatments were detected from week 2 until the end of the season showing the divergence in plant height across irrigation treatments for the majority of the growing season. Tables 5 A and B show the results of the ANOVA and Tukey's test for the sorghum maturity-stage CHM that was collected on 10/05/21.

Table 5.

A. The maturity stage TLS-generated mean canopy height model (CHM) ANOVA of the white and red varieties of sorghum in response to 3 levels of deficit irrigation. This crop phenotyping study was conducted at the UNR CABNR Valley Road Laboratory, Reno, NV.

Source: White Red	DF	SS	MS	F	P
Treatment	2	71.5	35.76	533.2	2e-16
	2	63.6	31.81	647.4	2e-16
Residuals	12120	812	0.07		
	11669	573.3	0.05		

B. Tukey Honest Significant Differences (HSD) test showing adjusted p-values.

Variety	Treatment	DF	LWR	UPR	P-Adj
White Red	100-60 100-60	0.132 0.124	0.119 0.113	0.146 0.136	0 0
White Red	100-30 100-30	0.183 0.177	0.169 0.165	0.197 0.189	0 0
White Red	60-30 60-30	0.051 0.053	0.038 0.041	0.064 0.065	0 0

3.2 TLS 2022

The 2022 mean CHM phenology for the growing season shows a similar, but slightly different

growth pattern than the 2021 season (Figure 7 A and B). Both varieties showed two periods of rapid

growth before plateauing in mid to late August.
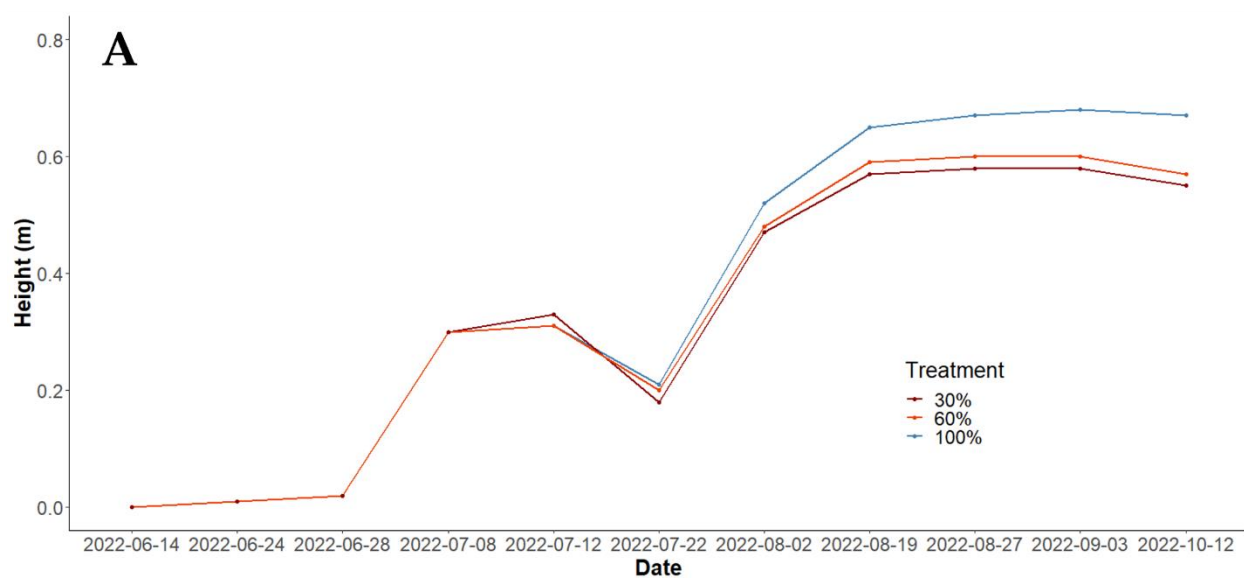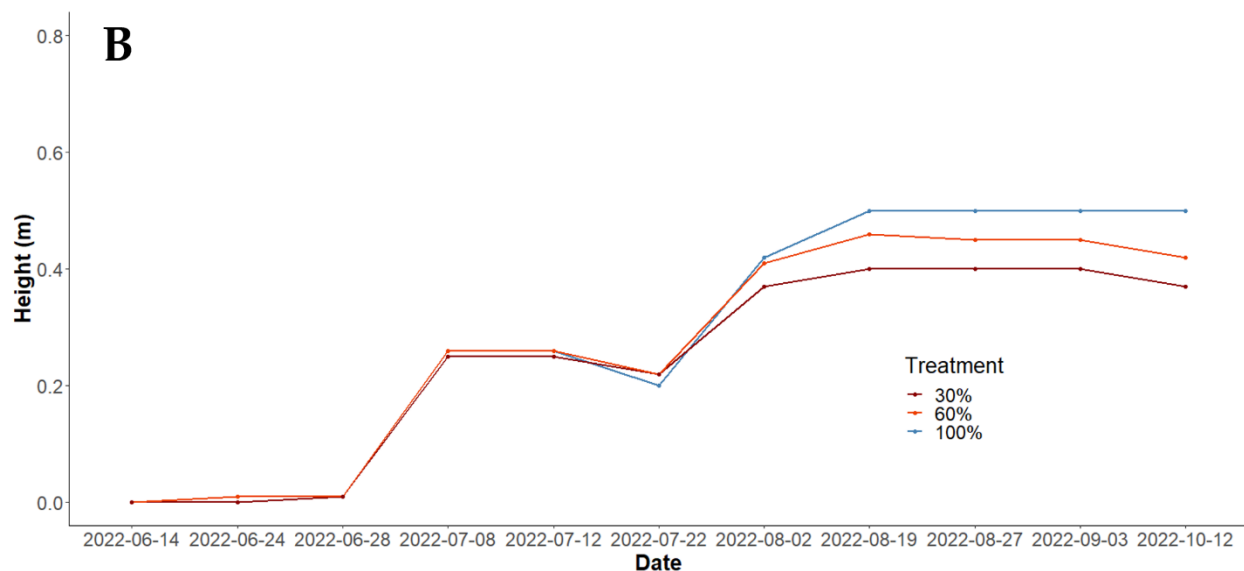
Figure 6. The 2022 TLS-generated mean canopy height model (CHM) for the white (A) and red (B) varieties of sorghum in response to 3-levels of deficit irrigation versus TLS collection dates indicate the phenology of the two varieties. The July 22, 2022 "dip" is probably reflective of the impact of wild bird granivores. This crop phenotyping study was conducted at the UNR CABNR Valley Road Laboratory, Reno, NV.

3.2.1 White

TLS ANOVA results of the white variety for 2022 showed no significant differences in height across any treatments until scan 7 on 7/12/22. Significant differences in height were detected for both the 100-30% and 60-30% treatments. All 3 treatments showed a divergence in height (p-values < 0.05) on the following scan on 7/22/22. This trend continued until the end of the season. ANOVA and Tukey's results for the final data collection of 10/12/22 are displayed in Table 6. The full section of ANOVAs for each collection can be found in Appendix A3.

3.2.2 Red

TLS ANOVA results for the red variety of 2022 showed a slight divergence in height differences of the 100-60% irrigation on 6/24/22, but these differences in height then disappeared after this point and did not show up again until 7/8/22 where all three treatments displayed significant differences in height.

Height differences across treatments would then fluctuate until the end of the season where clear

differences in height were apparent. ANOVA and Tukey's results for the final data collection of 10/12/22

in Table 6 show a clear difference in mean height across all three treatments. The full section of ANOVAs

for each week of scanning can be found in Appendix A4.

Table 6.

A. The maturity stage TLS-generated mean canopy height model (CHM) ANOVA of the white and red varieties of sorghum in response to 3 levels of deficit irrigation. This crop phenotyping study was conducted at the UNR CABNR Valley Road Laboratory, Reno, NV.

Source: White Red	DF	SS	MS	F	P
Treatment	2	19.1	9.566	177.5	2e-16
	2	14.08	7.041	213.1	2e-16
Residuals	6199	334.1	0.054		
	6485	214.3	0.033		

B. Tukey Honest Significant Differences (HSD) test showing adjusted p-values.

Variety	Treatment	Diff	LWR	UPR	P-Adj
White Red	100-60 100-60	0.09 0.05	0.073 0.037	0.107 0.063	0 0
White Red	100-30 100-30	0.135 0.115	0.117 0.102	0.152 0.128	0 0
White Red	60-30 60-30	0.045 0.065	0.027 0.052	0.062 0.078	0 0

3.3 GPR 2021

Mean amplitude reflectivity shows higher values for the 30% irrigation treatment and trends downward for the 60% and 100% (Figure 8 A and B). A possible growth curve is noted beginning on 7/28/21 as values trend upwards overall.
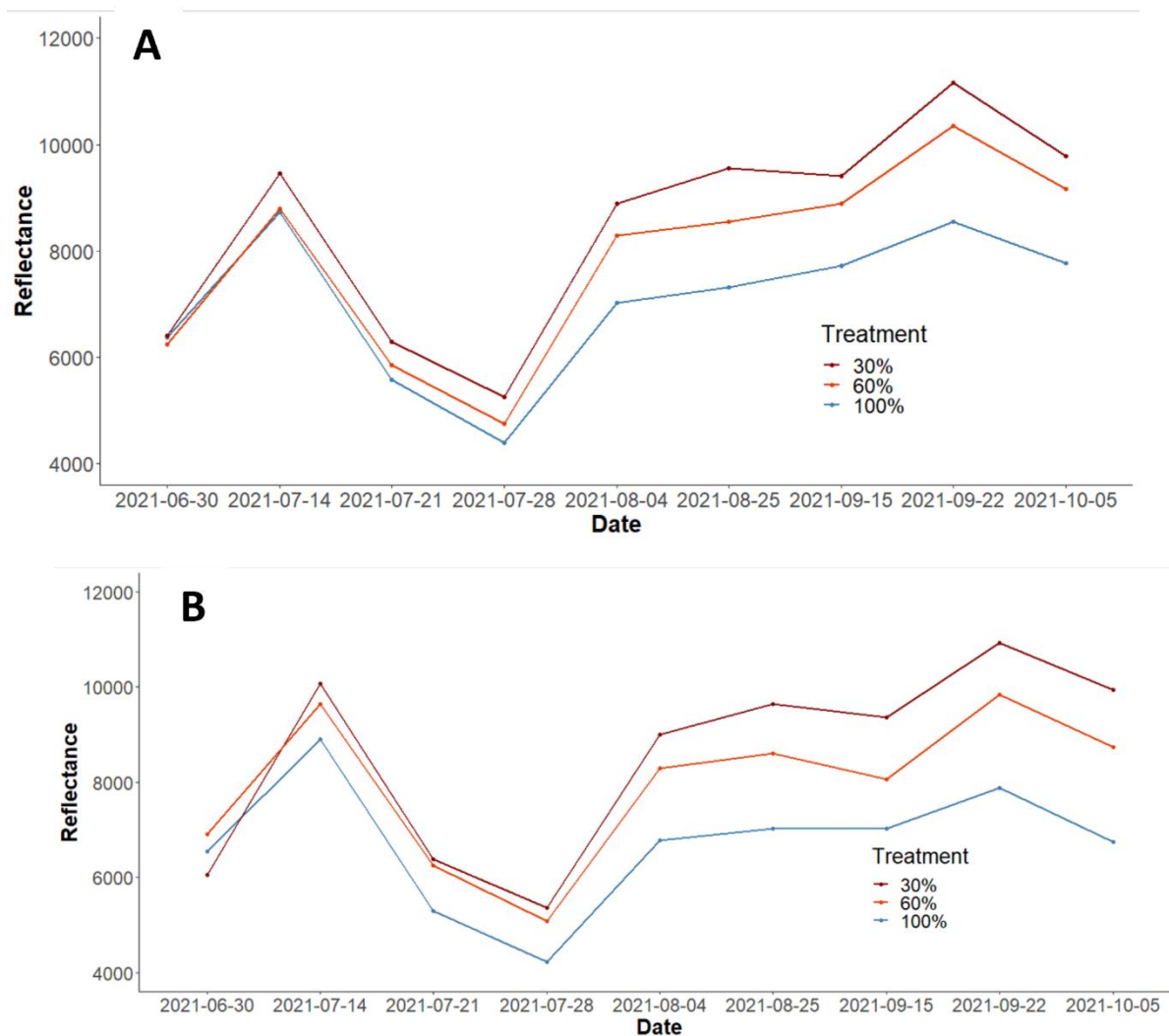
Figure 7. Ground penetrating radar (GPR) mean amplitude reflectivity of the white (A) and red (B) varieties of sorghum's root zone over the 2021 growing season in response to 3 levels of deficit irrigation. This crop phenotyping study was conducted at the UNR CABNR Valley Road Laboratory, Reno, NV.

3.3.1 White

GPR (ANOVA) showed a significant difference (p-value of near zero) between each treatment plot for the white varieties on the first week of data collection and continued for each consecutive week. Table 7 shows the results of the final GPR collection at the above-ground maturity stage of sorghum on

10/5/21 with strong differences in mean amplitude reflectivity. Repeated measures ANOVAs for the

entire growing season for the 2021 white variety can be found in Appendix A5.

3.3.2 Red

Similar to the white variety, radar reflectance for the red variety of sorghum showed an

immediate difference beginning at week 1 and continuing for the duration of the season. ANOVA results

are reported for the 10/5/21 red variety in Table 7. ANOVAs for the entire growing season for the 2021

red variety can be found in Appendix A6.

Table 7.

A. The 2021 GPR mean amplitude reflectivity ANOVA at the maturity stage of growth for the red and white varieties of grain sorghum in response to 3 levels of deficit irrigation. This crop phenotyping study was conducted at the UNR CABNR Valley Road Laboratory, Reno, NV.

Source: White Red	DF	SS	MS	F	P
Treatment	2 2	3.18e+09 9.467e+09	1.59e+09 4.73e+09	1780 6546	0 0
Residuals	5521 5099	4.94e+09 3.69e+09	8.95e+09 7.23e+05		

B. Tukey Honest Significant Differences (HSD) test showing adjusted p-values.

Variety	Treatment	Diff	LWR	UPR	P-Adj
White Red	100-60 100-60	-1198.196 -1898.615	-1269.515 -1968.252	-1126.878 -1828.977	0 0
White Red	100-30 100-30	-1764.136 -3213.327	-1837.084 -3279.539	-1691.188 -3147.115	0 0
White Red	60-30 60-30	-565.9402 -1314.713	-645.432 -1384.878	-486.448 -1244.547	0 0

3.4 GPR 2022

Figure 9 shows a similar pattern of GPR reflectance values for 2022 to 2021. The three treatments diverge with 30% having highest reflectance followed by 60% then 100%. A similar curve appears in the data beginning on 8/10/22 trending upwards.
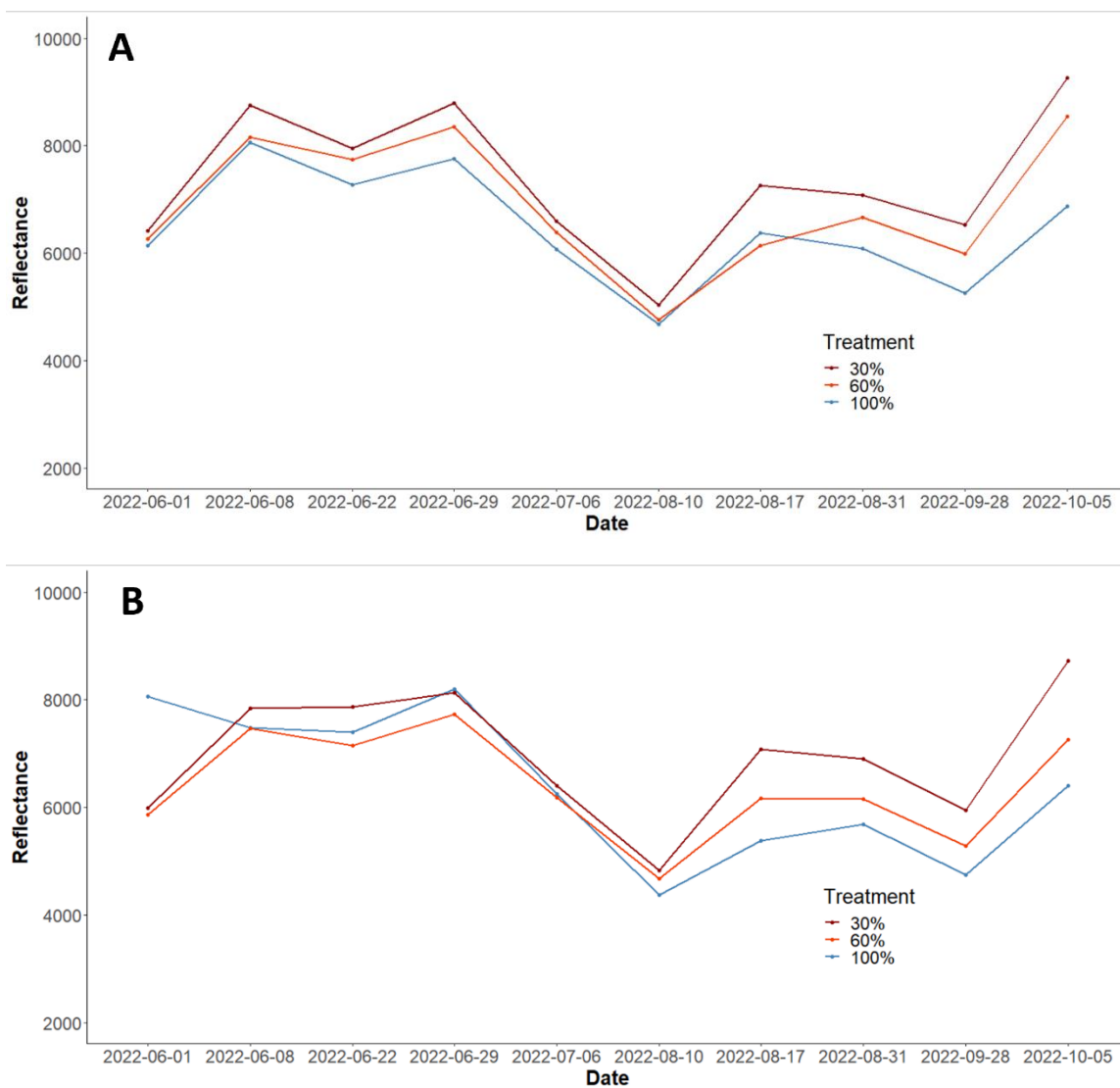
Figure 8. Ground penetrating radar (GPR) mean amplitude reflectivity of the white (A) and red (B) varieties of sorghum's root zone over the 2022 growing season in response to 3 levels of deficit irrigation. This crop phenotyping study was conducted at the UNR CABNR Valley Road Laboratory, Reno, NV.

3.4.1 White

The ANOVA results for the 2022 white variety show an immediate significant difference at the first week of collection. These statistical differences continue over the growing season and can be viewed in Appendix A7. Table 8 shows the results of the ANOVA for the above-ground maturity stage of sorghum data collection on 10/05/22

3.4.2. Red

Statistical analysis of the red variety for the 2022 season follows the same trend as the white variety with significant differences detected in the first week of data collection and continuing on for the course of the season. Appendix A8 shows the results of each ANOVA. The results of the final data collection on 10/05/22 are displayed alongside the white variety in table 8.

Table 8.

B. The 2022 GPR mean amplitude reflectivity ANOVA at the maturity stage of growth for the red and white varieties of grain sorghum in response to 3 levels of deficit irrigation. This crop phenotyping study was conducted at the UNR CABNR Valley Road Laboratory, Reno, NV.

Source: White Red	DF	SS	MS	F	P
Treatment	2	5.259e+09	2.629e+09	1700	2e-16
	2	3.473e+09	1.736e+09	1331	2e-16
Residuals	6867	1.062e+10	1.547e+06		
	7240	9.443e+09	1.304e+06		

B. Tukey Honest Significant Differences (HSD) test showing adjusted p-values.

Variety	Treatment	Diff	LWR	UPR	P-Adj
White Red	100-60 100-60	-2040.373 -1544.438	-2125.877 -1620.205	-1954.8695 -1468.671	0 0
White Red	100-30 100-30	-452.548 -185.871	-538.213 -263.225	-366.784 -108.516	0 0
White Red	60-30 60-30	1587.825 1358.567	1500.438 1280.195	1675.212 1436.94	0 0

3.5. Time series NDVI 2021

The Mean NDVI value time series for each variety of sorghum over the course of the growing season displayed rapid growth to peak values that then plateaued in late September as the panicles reached the maturity stage and the leaf blades began to dry out (Figure 9). NDVI values were greater in the 100% irrigation treatment with comparable though a lower performance at the 60% irrigation and a noticeable increase in NDVI at the maturity growth stage at the 30% irrigation level.
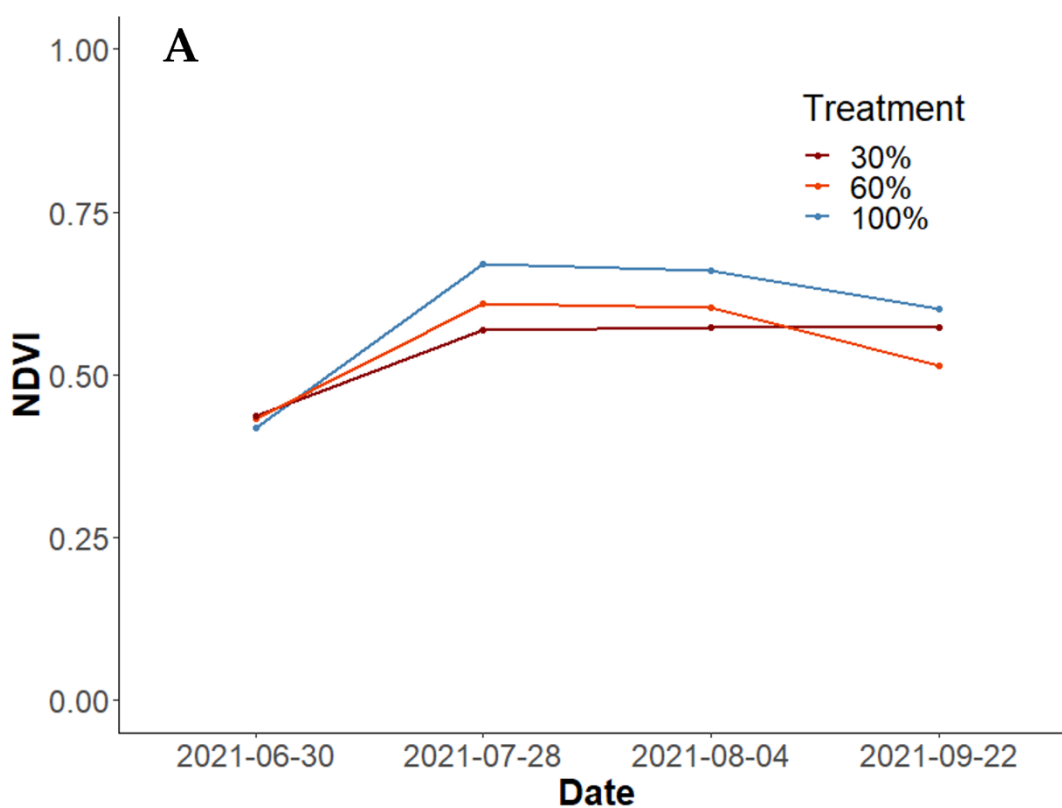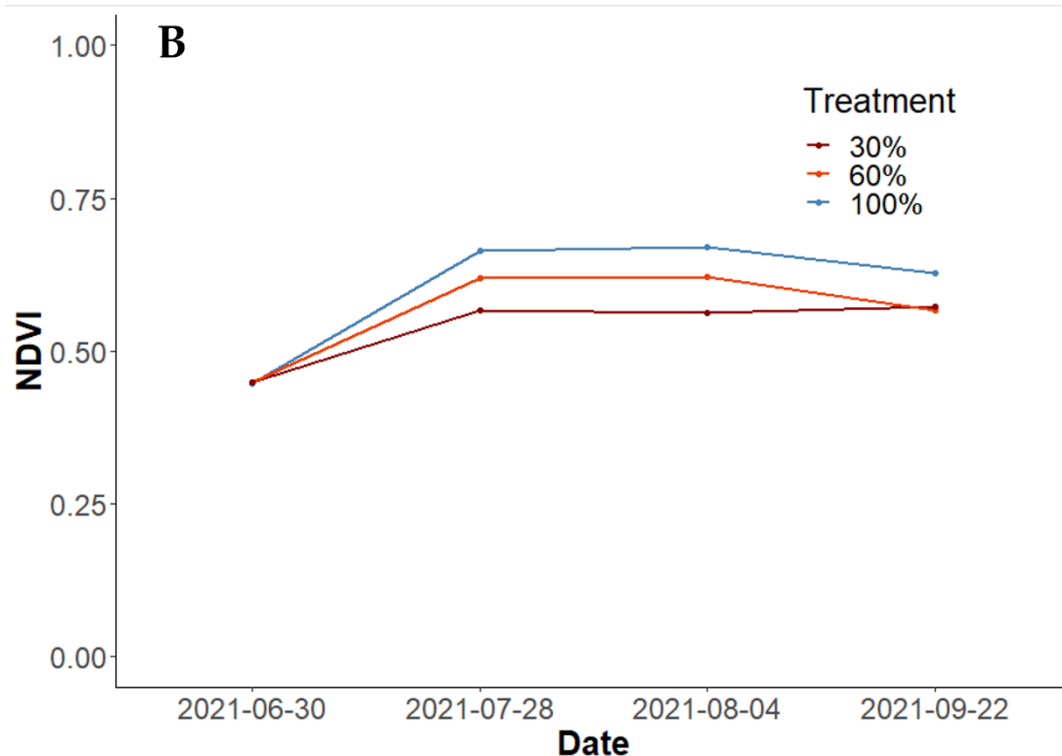
Figure 9. The mean normalized difference vegetation index (NDVI) of the white (A) and red (B) varieties of sorghum's canopy over the 2021 growing season in response to 3 levels of deficit irrigation. This crop phenotyping study was conducted at the UNR CABNR Valley Road Laboratory, Reno, NV.

3.5.1 White

ANOVA results for the 2021 white variety of NDVI collected on 9/22/21 are displayed below

(Table 9). These results show significant differences across all three treatments.

3.5.2 Red

Much like the white variety, the 2022 red variety of sorghum showed significant differences in

NDVI values between the three treatments for the final NDVI data collection on 9/22/21. Table 9 shows

the full ANOVA for the red variety alongside the white.

Table 9.

A. The 2021 normalized difference vegetation index (NDVI) ANOVA at the maturity stage of growth for the red and white varieties of grain sorghum in response to 3 levels of deficit irrigation. This crop phenotyping study was conducted at the UNR CABNR Valley Road Laboratory, Reno, NV.

Source: White Red	DF	SS	MS	F	P
Treatment	2 2	44.9 36.3	22.44 18.168	563.1 383.4	2e-16 2e-16
Residuals	14156 13421	564.1 635.9	0.04 0.047		

B. Tukey Honest Significant Differences (HSD) test showing adjusted p-values.

Variety	Treatment	Diff	LWR	UPR	P-Adj
White Red	100-60 100-60	0.104 0.076	0.094 0.066	0.113 0.087	0 0
White Red	100-30 100-30	0.133 0.127	0.123 0.116	0.143 0.138	0 0
White Red	60-30 60-30	0.029 0.050	0.02 0.04	0.039 0.061	0 07

3.6. Time series NDVI 2022

Figure 10 shows the time series of mean NDVI values collected over the two varieties of sorghum over the course of the growing season. Much like the previous season of 2021, each NDVI value rapidly increased in response to the drought treatments before plateauing by August. Differences in the three NDVI values in response to the drought treatments are visible by August and are maintained for the duration of the season, with the exception of the red variety. At sorghum's maturity stage in the growing season, the red variety shows a rapid increase in NDVI overtaking the other 2 treatments.
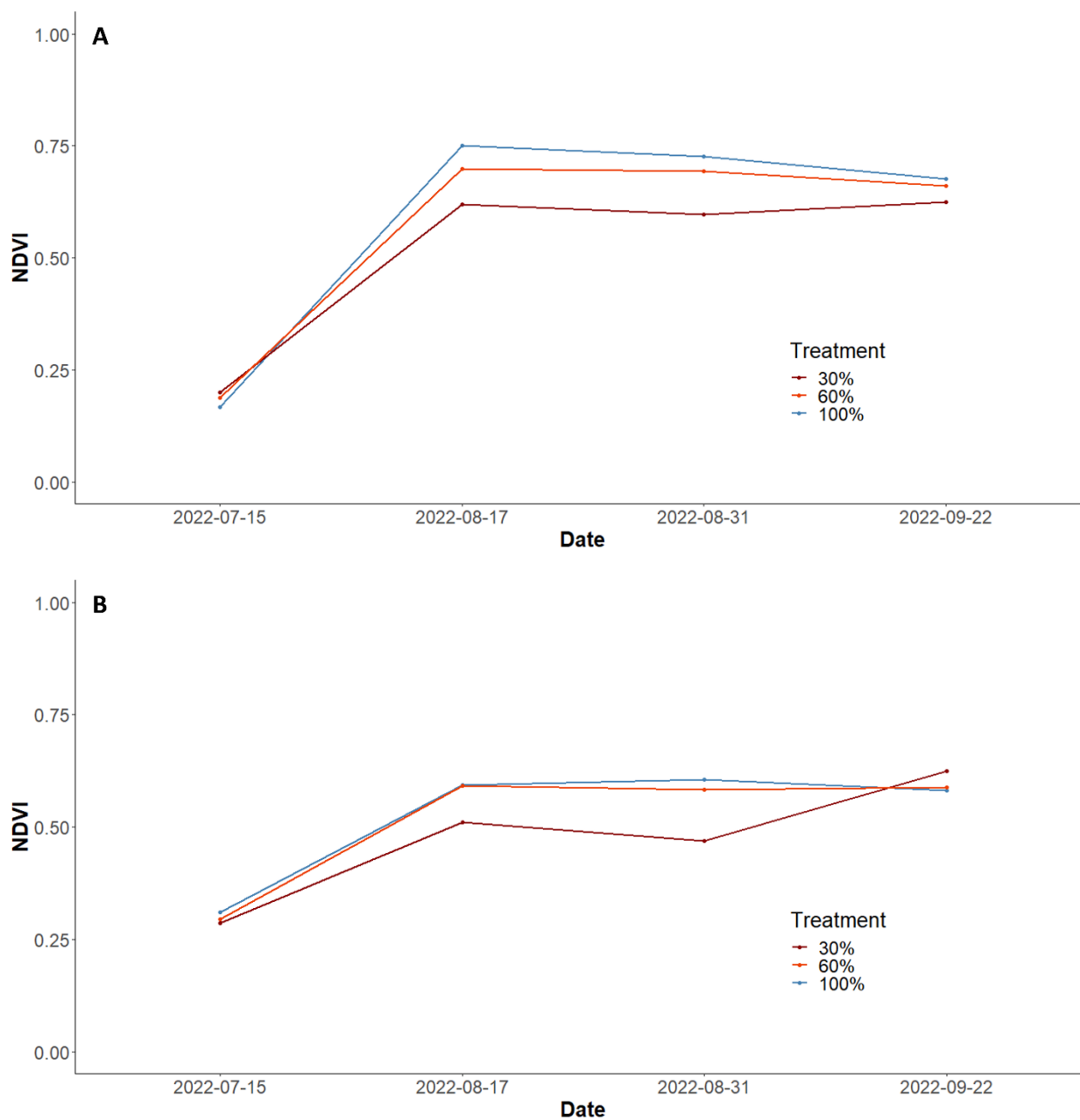
Figure 10. The mean normalized difference vegetation index (NDVI) of the white (A) and red (B) varieties of sorghum's canopy over the 2022 growing season in response to 3 levels of deficit irrigation. This crop phenotyping study was conducted at the UNR CABNR Valley Road Laboratory, Reno, NV.

3.6.1 White

The 2022 NDVI ANOVA results for the white variety of sorghum showed significant differences only between the 100 % and 30% deficit irrigation treatments, but not for the other treatments (Table 10).

3.6.2 Red

The 2022 NDVI ANOVA results for the red variety of sorghum were strikingly different from the

white variety with significant differences across all three levels of deficit irrigation (Table 10 B).

Table 10.

A. The 2022 normalized difference vegetation index (NDVI) ANOVA at the maturity stage of growth for the red and white varieties of grain sorghum in response to 3 levels of deficit irrigation. This crop phenotyping study was conducted at the UNR CABNR Valley Road Laboratory, Reno, NV.

Source: White Red	DF	SS	MS	F	P
Treatment	2	0.32	0.158	4.22	0.015
	2	1.08	0.538	15.01	3.1e-07
Residuals	5710	213.70	0.037		
	5713	204.80	0.036		

B. Tukey Honest Significant Differences (HSD) test showing adjusted p-values.

Variety	Treatment	Diff	LWR	UPR	P-Adj
White Red	100-60 100-60	0.013 -0.017	-0.001 -0.031	0.03 -0.003	0.091 0.013*
White Red	100-30 100-30	0.018 0.017	0.003 0.003	0.033 0.031	0.015* 0.015*
White Red	60-30 60-30	0.005 0.034	-0.01 0.02	0.02 0.049	0.716 1.0e-05*

3.7 True Biomass

The 100% deficit irrigation treatment had the greatest aboveground wet biomass for the red (~65

kg) and white (~78 kg) varieties followed by the 60% treatment (red = 55 kg and white = 68 kg) and then

the 30% ((red = 45 kg and white = 54 kg, Figure 11). The belowground wet biomass showed a different

response pattern from the above-ground findings where 60% irrigation had the highest biomass followed

by the 100% then 30% (Figure 12).
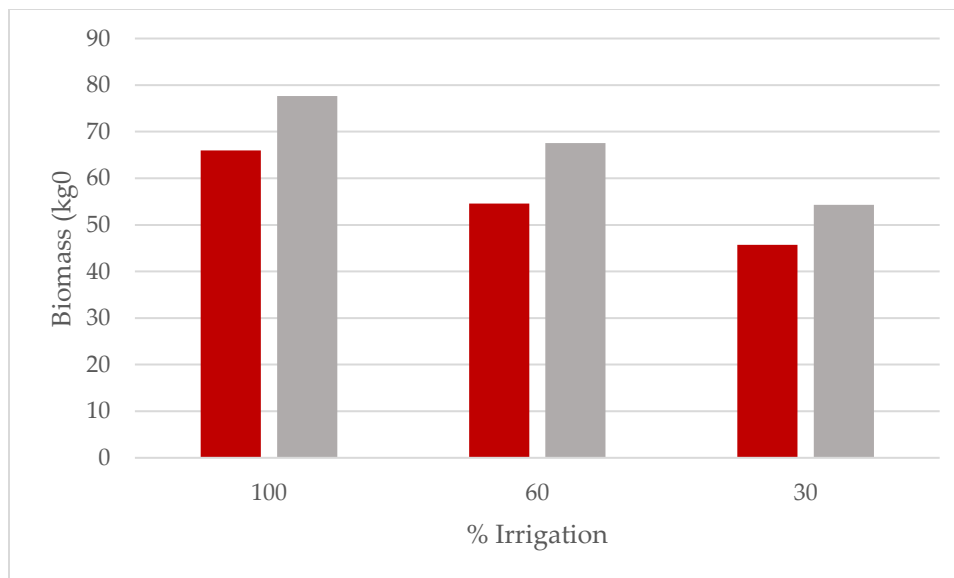
Figure 11. Total aboveground biomass in wet weight for the red and white varieties of grain sorghum in response to 3 levels of deficit irrigation. This crop phenotyping study was conducted at the UNR CABNR Valley Road Laboratory, Reno, NV.
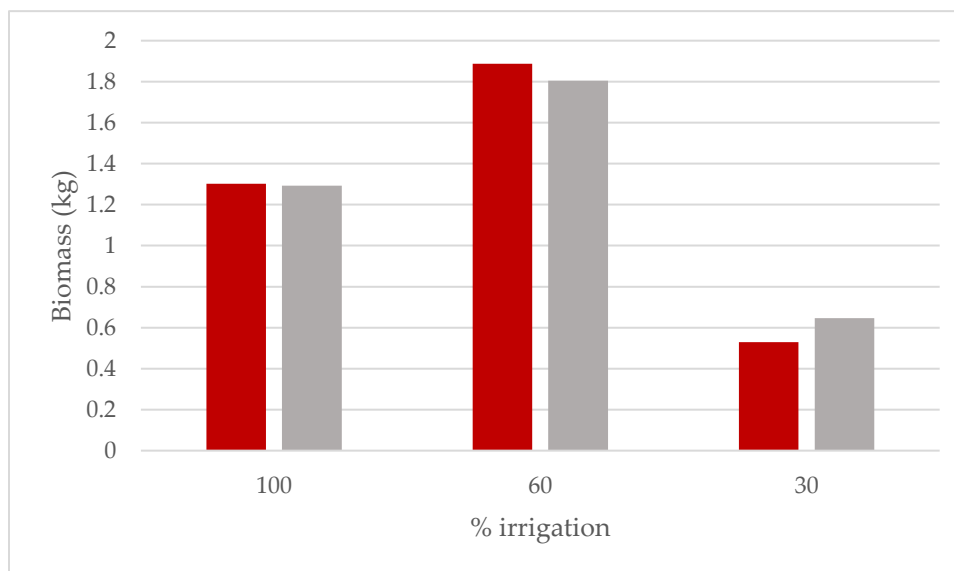
Figure 12. Estimated total belowground wet biomass for the red and white varieties of grain sorghum in response to 3 levels of deficit irrigation. This crop phenotyping study was conducted at the UNR CABNR Valley Road Laboratory, Reno, NV.

3.8 Random Forest and Regressions

The results of the random forest spatial modeling to predict above ground biomass showed moderate capability. Of the 3 predictor variables used, mean CHM or plant height had the highest influence, followed by NDVI, and finally the red edge index (Figure 12). The best model fit resulted in an R^2 of 0.133, a root mean square error (RMSE) of 32.8, and an the mean absolute error (MAE) of 25.1. These results indicate that this particular RF model had a poor correlation with actual aboveground biomass with a mean difference between predicted and actual biomass of 25 g.

Variable Importance for Biomass Prediction
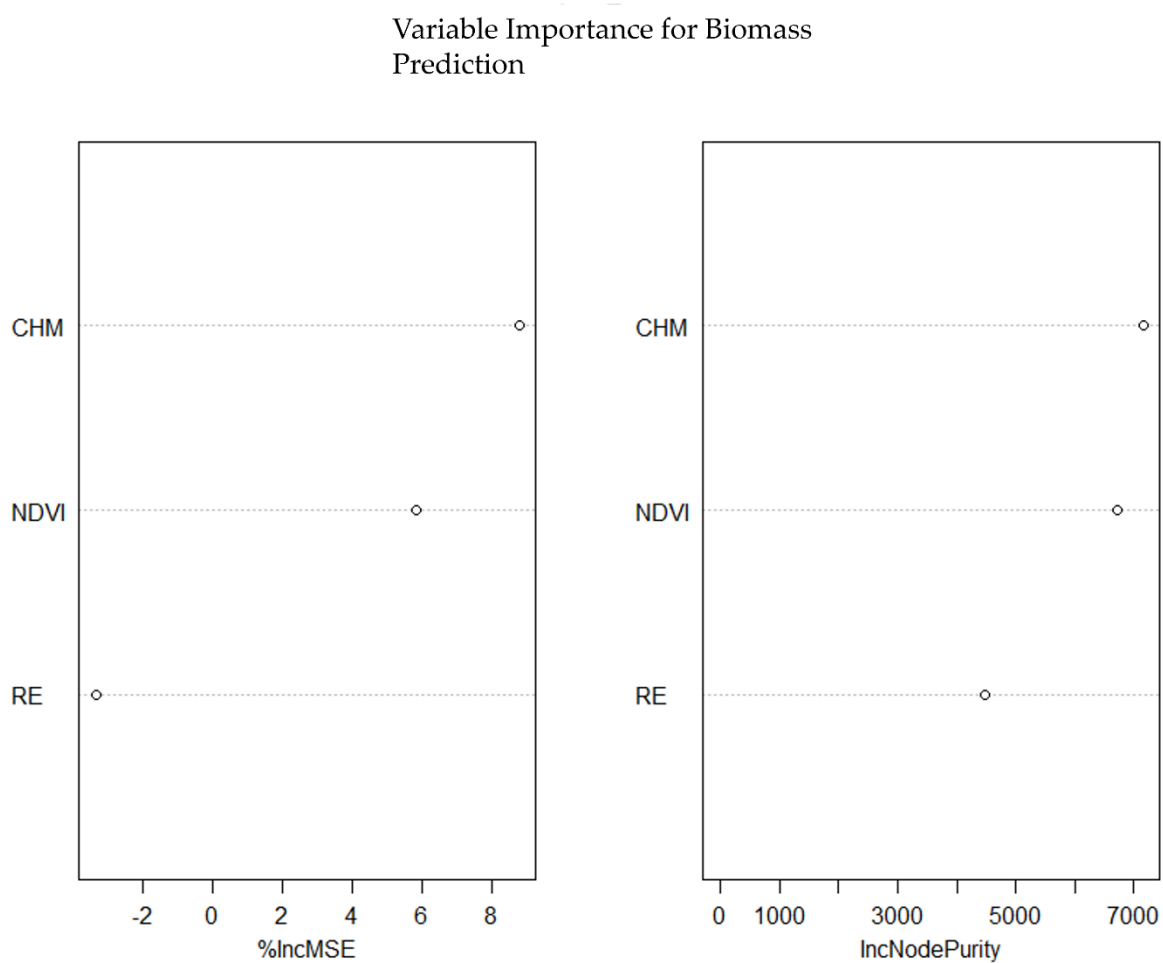
Figure 13. The Importance and MSE plots for the random forest model's 3 remote sensing predictors, two from the multispectral camera (NDVI and red edge NDVI) and one from the TLS, i.e., the canopy height model (CHM) at the maturity growth stage of sorghum. The predictors are used to predict biomass across the two varieties. This crop phenotyping study was conducted at the UNR CABNR Valley Road Laboratory, Reno, NV.

4. Discussion

4.1. TLS

The time series analysis of vegetation height phenology for this study accurately tracked the response of sorghum crop height for the two varieties in response to deficit irrigation over two growing seasons using the Leica C10 laser scanner. We predicted that differences in vegetation height would be detectable across the three treatments and that the heights would decrease in accordance with deficit irrigation and this trend was confirmed. Our results showed a clear difference in plant height between the control (100%) and both deficit treatments (60%,30%), proving the capability of TLS to accurately monitor plant height and structure. The canopy height models (CHM) were able to measure plant height over both growing seasons and even captured the loss in vegetation height that occurred due to the bird granivores that occurred in late July for both field seasons, particularly the 2022 season. Terrestrial laser scanning provides a highly accurate means for plant monitoring over a broad range of health metrics.

Our lidar-derived CHMs proved to be highest in importance for estimating plant biomass and significant differences between treatments were detected. The CHM derived from the final data collection of the 2022 season appears to correlate with the harvested aboveground biomass (Figure 14). This work reinforces the capability of lidar for vegetation monitoring.
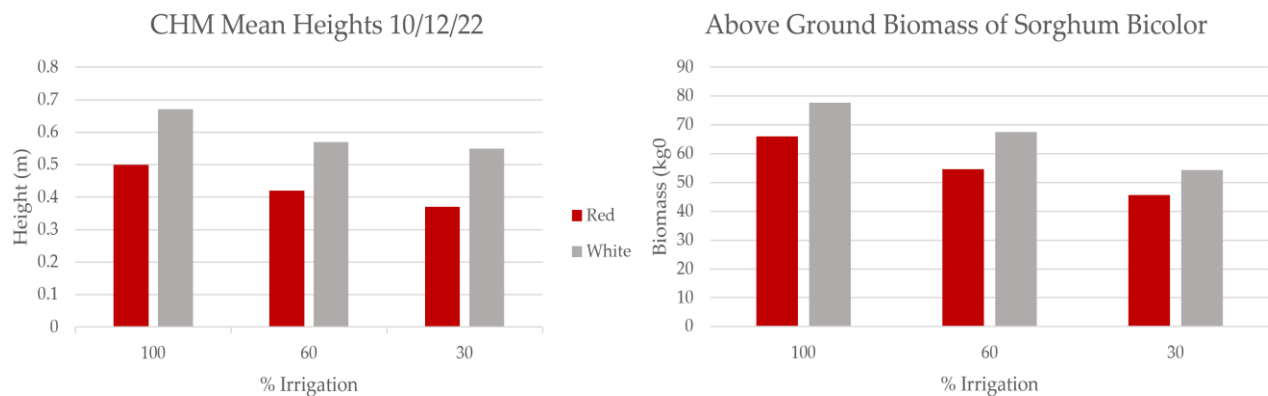
Figure 14. The mean plant height by treatment and mean biomass by treatment.

4.2. GPR

We predicted that differences in radar reflectance would be detectable across the three irrigation treatments, and that larger root masses would be detected in the 30% to 60% deficit irrigation treatments. Following the principle that relative permittivity is inversely related to radar velocity, our results showed greater biomass levels in the 100% and 60% than the 30% irrigation. Our ground sampled root biomass reflects a similar pattern with 60% having the highest biomass levels followed by the 100% and then 30%. Figure 16 shows radar reflectance and sampled biomass allowing a side-by-side comparison. These results indicate that drought-stressed sorghum bicolor does produce greater root masses as we predicted, but there is a limit or threshold before the plants begin to struggle to grow entirely. The 60% irrigation treatment had the greatest root biomass though this difference wasn't fully detected in the radar reflectance. The results of the mean radar reflectance over time show that we successfully were able to detect changes in belowground biomass as the plants matured.

Statistically significant differences were detected across all three treatments, but this could be due to the use of ANOVAs. This level of significant difference from the first week of scanning is possibly due to the ANOVA's sensitivity to population size. Small levels of variance within a population can be amplified by the sheer volume of occurrences creating artificially small p-values despite the coarsening of data to 20 cm resolution which was judged to be close to the mean diameter of a sorghum root mass The high resolution of the radar data inflates the population size for each treatment, despite the data being coarsened to 20 cm resolution. The 20 cm grid size was chosen as it closely matched the mean diameter of the sampled mature root mass. Further work must be done to evaluate differences in the radar data at coarser and finer scales to estimate how well the GPR is laterally detecting the root masses. Analyzing the mean amplitude reflectivity data gives us a better understanding of how drought stress affects the root masses and their detection in the radar data. The 100% and 60% irrigation treatments commonly had

similar amplitude values with the 100% being consistently lower than the 60%. This would indicate that larger root masses are being detected in the 100% irrigation as radar velocity is inversely proportional to relative permittivity and root water content. Further analysis of the 100% and 60% deficit irrigation treatments in conjunction with field sampled belowground biomass is ongoing.
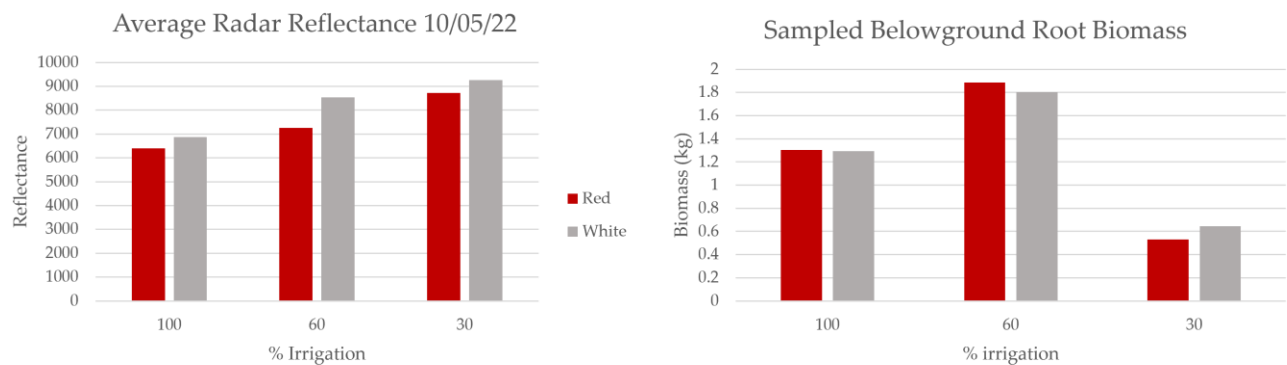
Figure 15. Mean radar reflectance for 10/05/22 and sampled belowground biomass.

4.3. UAV Multispectral

The spectral dataset provided by the MicaSense Altum camera allowed us to generate extremely high-resolution orthomosaics of several different spectral indices. The two primary indicators used were the NDVI and a red edge index based on the same formula used for NDVI. Both indices target the near-infrared (NIR) region of the electromagnetic spectrum, though the red edge band is specifically designed to target the region of the highest NIR reflectance in vegetation. UAV photogrammetry can also be used to derive 3D structural datasets through the use of structure from motion (SfM) methodology, though this was not needed for our study in addition to the Lidar datasets.

We predicted that higher NDVI values would be detected in the 100% irrigation and would decrease accordingly as irrigation was decreased. The resulting NDVI values of our UAV data accurately tracked the crop growth cycle over time and was capable of detecting differences in NDVI across the

three treatments following our expectations. The 100% irrigation showed the highest NDVI values over

the course of the growing season for both years and decreased in levels in accordance with % irrigation,

though less so in the red variety. Mean NDVI values for the final data collection on 9/22/22 show the

expected 100-60-30% downward trend for the white variety. The red variety showed a near equal level for

100% and 60% and an increase in the 30% irrigation. Mean NDVI and total aboveground biomass show

how NDVI can be useful for vegetation monitoring, but does not always equivalate to biomass (Figure

17). NDVI was second in importance in the random forest biomass estimation indicating its potential for

modelling on broader scales.
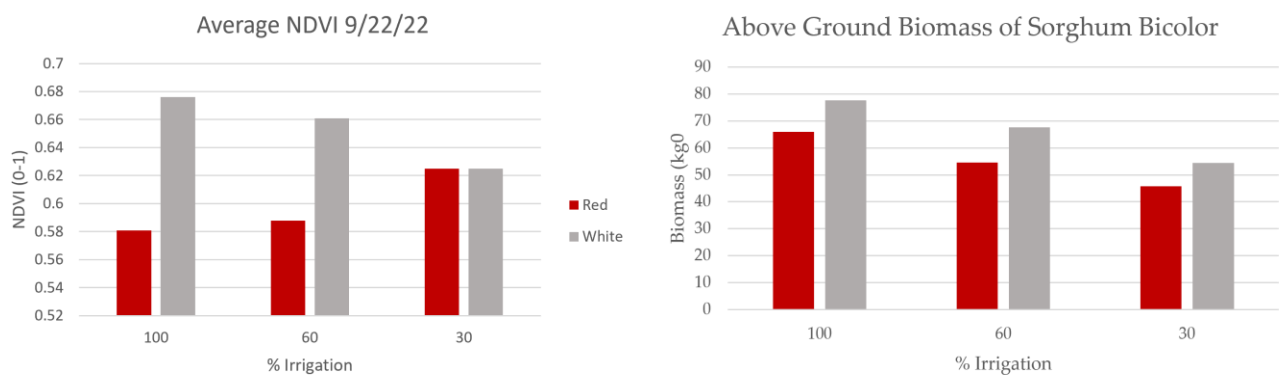
Figure 16. Mean NDVI for 9/22/22 and aboveground biomass by % irrigation.

4.4 sUAS flight issues

The launch version of the Micasense Altum struggles at capturing photos faster than a 2 second

interval when flown at low altitude, which was unknown during the first season of data collection. The

recommended flight altitude for the Micasense Altum is no lower than 30 meters above ground level

(AGL), however, altitudes above 15 m did not generate high enough resolution pixels for our purposes.

Further issues with airspace clearance occurred during the 2022 field season. Airspace access was

extremely limited during this time due to a change in airspace from 30m AGL to 0 m by the Federal

Aviation Administration (FAA). This required us to file waivers through the FAA weekly for manual

approval by Reno air traffic control. Because of these changes, fewer flights were employed than were

preferred.

4.5. Biomass predictive models

A random forest model for predicting aboveground biomass was created using the canopy height model

(CHM), the UAV-derived normalized difference vegetation index (NDVI), and a Red Edge vegetation

index as predictive variables. Previous studies have used UAV-based multispectral vegetation indices

such as NDVI for biomass prediction with limited accuracy **[34]**. Other studies have used airborne lidar-

derived metrics such as height and crown diameter for tree biomass prediction with some success **[35]**.

We predicted that the lidar-derived CHM would most accurately reflect biomass and that the red edge

band would perform better than traditional NDVI given its purpose in vegetation monitoring. Our model

employed both vegetation height as well as two vegetation indices with limited results. A low R^2 of 0.133

indicates poor correlation of predictors to actual and MAE of 25.1 showing that our predictor model was

unable to accurately predict above-ground biomass to a high degree of accuracy. Plant height had the

greatest importance in the model followed by NDVI and then the red edge index. This comes as a

surprise as the red edge band is designed to target the rapid change in near-infrared reflectance of

vegetation [36,37]. Further work utilizing other machine learning algorithms and other predictor

variables is required to accurately model plant biomass.

4.6 Linear modeling of belowground biomass using GPR

The simple linear regression was not statistically significant and did not linearly correlate radar

reflectance and belowground biomass. This was not overly surprising as our methods for radar

processing were primarily aimed at plot level estimates and the belowground biomass was harvested

only over 0.5 m^2 areas. A full accounting of plot level belowground biomass regressed against plot level radar reflectance would hopefully show a better relationship, but retrieving that much biomass requires a time investment currently unavailable to us.

5. Conclusions

Terrestrial laser scanning has been used numerous times to accurately assess a whole host of vegetation monitoring such as plant height [38], cover, yield, and biomass to name a few [15,39,40]. Other uses of Lidar for vegetation monitoring have been employed through the use of airborne vehicles such as Asner's 3D vegetation structure and height monitoring [41].

The lidar-derived CHM's accurately tracked plant height over the entire growing season. The utility of high-resolution lidar for collecting several different structural metrics out of a single dataset is incredibly useful for all types of vegetation monitoring. Airborne lidar has been applied for broadscale vegetation monitoring at high resolution in African savannas [41] to great success. Terrestrial lidar, while more limited in scope, can produce extremely high-accuracy 3D models of the subject matter that can be used to determine plant height as well as other metrics such as volume and structure.

Ground penetrating radar's use in agriculture is still largely in its infancy. There have been several cases of its use in detecting coarse tree roots or tubers [20,21] where the GPR was moved over these coarse roots in different directions creating a hyperbolic response in the raw radargram data. This method allows researchers to relate the size of each hyperbolic response to a known amount of biomass and works well for roots above a certain diameter. For roots smaller than that limit, or in the case that the GPR cannot be moved directly over the root mass, new methods of data processing must be employed. For this study, we relied on the wide swath width of the GPR to detect changes over time in the root mass from a lateral view.

The use of ground penetrating radar in agriculture is still largely nascent. Some of the earliest publications by Butnor in 2001 [21] on coarse root detection established the methodology that would be used by numerous other researchers in the years since. This methodology relies on hyperbola detection of objects large enough to generate such a response. Our system of lateral root detection on smaller root diameters required the development of a novel approach utilizing the gridded (Velocity or amplitude) measures from a minimally filtered radargram. Our results show that we were successful in detecting root changes over time, but firmly establishing total biomass through these methods remains problematic. Further research is required to broaden the capabilities of this technology, though the recent use of airless GPR systems could possibly remove many of the obstacles present in air-sensitive systems.

Multispectral imagery in agriculture is of particular use due to the ease of access and efficiency of the technology. A single UAV can collect several different vegetation monitoring metrics at high resolution over multiple acres of landscape. This creates an easy point of entry for wide-scale vegetation monitoring, though there is the potential for difficulty as previously noted. The implementation of incorrect technology for the use case can create obstacles in data analysis and restrictions on airspace can be cumbersome to overcome.

Appendix 1

Week	Treatment (White)	p-value
1	100-60	0
	100-30	0
	60-30	0.0000008
2	100-60	0
	100-30	0
	60-30	0.205
3	100-60	0
	100-30	0
	60-30	0.955
4	100-60	0
	100-30	0
	60-30	0.146
5	100-60	N/A
	100-30	N/A
	60-30	N/A
6	100-60	0
	100-30	0
	60-30	0.000002
7	100-60	0
	100-30	0
	60-30	0.02
8	100-60	0
	100-30	0
	60-30	0
9	100-60	0
	100-30	0
	60-30	0
10	100-60	0
	100-30	0
	60-30	0

Table A1. 2021 TLS post hoc Tukey HSD of white variety reported p-values of each scan.

Week	Treatment (Red)	p-value

1	100-60	0
	100-30	0
	60-30	0.994
2	100-60	0
	100-30	0
	60-30	0.008
3	100-60	0
	100-30	0
	60-30	0
4	100-60	0
	100-30	0
	60-30	0
5	100-60	N/A
	100-30	N/A
	60-30	N/A
6	100-60	0
	100-30	0
	60-30	0
7	100-60	0
	100-30	0
	60-30	0
8	100-60	0
	100-30	0
	60-30	0
9	100-60	0
	100-30	0
	60-30	0
10	100-60	0
	100-30	0
	60-30	0

Table A2. 2021 TLS post hoc Tukey HSD of red variety reported p-values of each scan.

Week	Treatment (White)	p-value
1	100-60	0.639

	100-30	0.277
	60-30	0.499
2	100-60	0996
	100-30	0.368
	60-30	0.385
3	100-60	0.777
	100-30	0.121
	60-30	0.33
4	100-60	0.449
	100-30	0.822
	60-30	0.186
5	100-60	0.831
	100-30	0.0001
	60-30	0.0008
6	100-60	2.5e-05
	100-30	3.15e-012
	60-30	1.45e-10
7	100-60	0
	100-30	0
	60-30	0
8	100-60	3.56e-12
	100-30	3.53e-12
	60-30	4.28e-08
9	100-60	0
	100-30	0
	60-30	1.97e-09
10	100-60	0
	100-30	0
	60-30	8.59e-09
11	100-60	1.62e-13
	100-30	1.62e-13
	60-30	3.21e-09

Table A3. 2022 TLS ANOVA of white variety reported p-values of each scan.

Week	Treatment (Red)	p-value

1	100-60	0.728
	100-30	0.999
	60-30	0.707
2	100-60	0.037
	100-30	0.086
	60-30	0.739
3	100-60	0.777
	100-30	0.121
	60-30	0.33
4	100-60	4.83e-09
	100-30	4.81e-09
	60-30	0.002
5	100-60	3.24e-08
	100-30	3.23e-08
	60-30	0.002
6	100-60	2.97e-07
	100-30	0.731
	60-30	1.88e-05
7	100-60	0.867
	100-30	0
	60-30	0
8	100-60	7.89e-06
	100-30	0
	60-30	0
9	100-60	7.94e-08
	100-30	3.84e-12
	60-30	3.87e-12
10	100-60	0.0001
	100-30	0
	60-30	0
11	100-60	0
	100-30	0
	60-30	0

Table A4. 2022 TLS ANOVA of red variety reported p-values of each scan.

Week	Treatment (White)	p-value
1	100-60	3.32e-08
	100-30	0.273
	60-30	3.31e-08
2	100-60	0.007
	100-30	3.47e-08
	60-30	3.47e-08
3	100-60	3.51e-08
	100-30	3.51e-08
	60-30	3.51e-08
4	100-60	0
	100-30	0
	60-30	0
5	100-60	3.32e-08
	100-30	3.32e-08
	60-30	3.32e-08
6	100-60	1.39e-09
	100-30	1.39e-09
	60-30	1.39e-09
7	100-60	0
	100-30	0
	60-30	0
8	100-60	0
	100-30	0
	60-30	0
9	100-60	1.01e-12
	100-30	1.01e-12
	60-30	1.01e-12

Table A5. 2021 GPR ANOVA of white variety reported p-values of each scan.

Week	Treatment (Red)	p-value
1	100-60	0
	100-30	0
	60-30	0
2	100-60	0

	100-30	0
	60-30	0
3	100-60	0
	100-30	0
	60-30	0
4	100-60	0
	100-30	0
	60-30	0
5	100-60	1.55e-13
	100-30	1.55e-13
	60-30	1.55e-13
6	100-60	1.15e-08
	100-30	1.15e-08
	60-30	1.15e-08
7	100-60	0
	100-30	0
	60-30	0
8	100-60	6.10e-09
	100-30	6.10e-09
	60-30	6.10e-09
9	100-60	0
	100-30	0
	60-30	0

Table A6. 2021 GPR ANOVA of red variety reported p-values of each scan.

Week	Treatment (Red)	p-value
1	100-60	7.74e-12
	100-30	7.74e-12
	60-30	0.02
2	100-60	2.63e-12
	100-30	2.63e-12
	60-30	4.09e-05
3	100-60	4.04e-12
	100-30	4.01e-12
	60-30	0.001

4	100-60	0
	100-30	0
	60-30	0
5	100-60	4.36e-08
	100-30	1.50e-07
	60-30	0.001
6	100-60	7.96e-06
	100-30	4.36e-08
	60-30	4.36e-08
7	100-60	5.68e-12
	100-30	0.0004
	60-30	5.68e-12
8	100-60	2.64e-12
	100-30	2.64e-12
	60-30	2.64e-12
9	100-60	3.72e-12
	100-30	3.72e-12
	60-30	3.72e-12
10	100-60	6.77e-12
	100-30	6.79e-12
	60-30	6.77e-12
11	100-60	7.26e-12
	100-30	7.29e-12
	60-30	7.26e-12
12	100-60	7.26e-12
	100-30	7.29e-12
	60-30	7.26e-12
13	100-60	3.87e-12
	100-30	3.87e-12
	60-30	3.87e-12

Table A7. 2022 GPR ANOVA of white variety reported p-values of each scan.

Week	Treatment (Red)	p-value
1	100-60	1.76e-12
	100-30	0.903

	60-30	1.76e-12
2	100-60	1.98e-12
	100-30	1.98e-12
	60-30	1.98e-12
3	100-60	1.13e-12
	100-30	0.003
	60-30	1.13e-11
4	100-60	4.68e-12
	100-30	4.72e-12
	60-30	4.68e-12
5	100-60	3.84e-08
	100-30	0.064
	60-30	3.84e-08
6	100-60	2.64e-08
	100-30	2.64e-08
	60-30	2.64e-08
7	100-60	7.94e-12
	100-30	0.002
	60-30	7.94e-12
8	100-60	2.02e-12
	100-30	0.323
	60-30	2.20e-12
9	100-60	9.10e-12
	100-30	9.10e-12
	60-30	9.10e-12
10	100-60	7.29e-12
	100-30	0.396
	60-30	7.29e-12
11	100-60	6.46e-12
	100-30	0.348
	60-30	6.46e-12
12	100-60	6.46e-12
	100-30	0.348
	60-30	6.46e-12
13	100-60	9.62e-12

	100-30	5.52e-08
	60-30	9.62e-12

Table A8. 2022 GPR ANOVA of the red variety's reported p-values for each scan.

Week	Treatment (White)	p-value
1	100-60	0.041
	100-30	0.176
	60-30	6.59e-05
2	100-60	1.80e-05
	100-30	0
	60-30	0
3	100-60	0.004
	100-30	3.08e-12
	60-30	3.10e-12
4	100-60	0.092
	100-30	0.015
	60-30	0.716

Table A9. 2022 NDVI ANOVA of white variety reported p-values

Week	Treatment (Red)	p-value
1	100-60	0.075
	100-30	4.48e-05
	60-30	0.084
2	100-60	0.706
	100-30	0
	60-30	0
3	100-60	0.2
	100-30	0
	60-30	0
4	100-60	0.013
	100-30	0.015
	60-30	1.34e-07

Table A10. 2022 NDVI ANOVA of red variety reported p-values

References

1. Robinson, N.P.; Allred, B.W.; Naugle, D.E.; Jones, M.O. Patterns of rangeland productivity and land ownership: Implications for conservation and management. *Ecological applications : a publication of the Ecological Society of America.* **2019**, *29*, doi:10.1002/eap.1862.
2. Havstad, K.; Peters, D.; Allen-Diaz, B.; Bartoiome, J.; Bestelmeyer, B.; Briske, D.; Brown, J.; Brunson, M.; Herrick, J.; Huntsinger, L., et al. The Western United States Rangelands: A Major Resource. **2009**, doi:10.2134/2009.grassland.c5.
3. Grove, A.T. WORLD ATLAS OF DESERTIFICATION, 2nd edition, edited by N. J. Middleton and D. S. G. Thomas, Arnold, London, 1997. No. of pages: x + 182. Price: £145.00 (hb). ISBN 0-340-69166-2. *Earth Surface Processes and Landforms* **1999**, *24*, 280-280, doi:https://doi.org/10.1002/(SICI)1096-9837(199903)24:3<280::AID-ESP955>3.0.CO;2-7.
4. Safriel, U.; Adeel, Z. Development paths of drylands: thresholds and sustainability. *Sustainability Science* **2008**, *3*, 117-123.
5. Zomer, R.J.; Trabucco, A.; Bossio, D.A.; Verchot, L.V. Climate change mitigation: A spatial analysis of global land suitability for clean development mechanism afforestation and reforestation. *Agriculture, ecosystems & environment* **2008**, *126*, 67-80.
6. Zomer, R.J.; Xu, J.; Trabucco, A. Version 3 of the global aridity index and potential evapotranspiration database. *Scientific Data* **2022**, *9*, 409.
7. Huang, J. Accelerated dryland expansion under climate change. Yu, H., Ed. 2016.
8. Delgado-Baquerizo, M.; Soliveres, S.; Hernández-Clemente, R.; Zhao, Y.; Gaitán, J.J.; Berdugo, M.; Delgado-Baquerizo, M.; Soliveres, S.; Hernández-Clemente, R.; Zhao, Y., et al. Global ecosystem thresholds driven by aridity. *Science.* **2020**, *367*, 787-790, doi:10.1126/science.aay5958.
9. Brandon Bishop, D.D. ECONOMIC ANALYSIS OF THE FOOD AND AGRICULTURE SECTOR IN NEVADA. Agriculture, N.D.o., Ed. Nevada Department of Agriculture, 2021.

10. Cramer, G.R.; Urano, K.; Delrot, S.; Pezzotti, M.; Shinozaki, K. Effects of abiotic stress on plants: a systems biology perspective. *BMC plant biology* **2011**, *11*, 1-14.
11. Famiglietti, J.S. The global groundwater crisis. *Nature Climate Change* **2014**, *4*, 945-948.
12. King, J. State-Engineer-Order-No.-1302-Diamond-Valley-Hydrographic-Basin-07-153-Eureka-County-Nevada. Nevada, O.O.T.S.E.O.T.S.O., Ed. Office of Nevada State Engineer: Carson City, 2019.
13. Chen, J.; Chopra, R.; Hayes, C.; Morris, G.; Marla, S.; Burke, J.; Xin, Z.; Burow, G. Genome-Wide Association Study of Developing Leaves' Heat Tolerance during Vegetative Growth Stages in a Sorghum Association Panel. *The plant genome* **2017**, *10*, plantgenome2016.2009.0091.
14. Mace, E.S.; Tai, S.; Gilding, E.K.; Li, Y.; Prentis, P.J.; Bian, L.; Campbell, B.C.; Hu, W.; Innes, D.J.; Han, X. Whole-genome sequencing reveals untapped genetic potential in Africa's indigenous cereal crop sorghum. *Nature communications* **2013**, *4*, 2320.
15. Eitel, J.U.; Vierling, L.A.; Long, D.S. Simultaneous measurements of plant structure and chlorophyll content in broadleaf saplings with a terrestrial laser scanner. *Remote sensing of Environment* **2010**, *114*, 2229-2237.
16. Eitel, J.U.; Magney, T.S.; Vierling, L.A.; Brown, T.T.; Huggins, D.R. LiDAR based biomass and crop nitrogen estimates for rapid, non-destructive assessment of wheat nitrogen status. *Field Crops Research* **2014**, *159*, 21-32.
17. Junttila, O.S.; Vastaranta, M.A.; Linnakoski, R.M.; Sugano, J.; Kaartinen, H.; Kukko, A.; Holopainen, M.E.; Hyyppä, H.; Hyyppä, J. Measuring leaf water content using multispectral

terrestrial laser scanning. *International Archives of the Photogrammetry, Remote Sensing & Spatial Information Sciences* **2017**.

18.   Guo, Q.; Su, Y.; Hu, T.; Guan, H.; Jin, S.; Zhang, J.; Zhao, X.; Xu, K.; Wei, D.; Kelly, M. Lidar boosts 3D ecological observations and modelings: A review and perspective. *IEEE Geoscience and Remote Sensing Magazine* **2020**, *9*, 232-257.

19.   Yang, W.; Feng, H.; Zhang, X.; Zhang, J.; Doonan, J.H.; Batchelor, W.D.; Xiong, L.; Yan, J. Crop phenomics and high-throughput phenotyping: past decades, current challenges, and future perspectives. *Molecular Plant* **2020**, *13*, 187-214.

20.   Delgado, A.; Hays, D.B.; Bruton, R.K.; Ceballos, H.; Novo, A.; Boi, E.; Selvaraj, M.G. Ground penetrating radar: a case study for estimating root bulking rate in cassava (Manihot esculenta Crantz). *Plant methods* **2017**, *13*, 1-11.

21.   Butnor, J.R.; Doolittle, J.; Kress, L.; Cohen, S.; Johnsen, K.H. Use of ground-penetrating radar to study tree roots in the southeastern United States. *Tree physiology* **2001**, *21*, 1269-1278.

22.   Center, W.R.C. UNR Valley Road Weather Station. Availabe online: **http://wrcc.dri.edu/page_name** (accessed on

23.   Staff, S.S. Web Soil Survey. Availabe online: https://websoilsurvey.sc.egov.usda.gov/App/WebSoilSurvey.aspx (accessed on

24.   *CloudCompare*, 2.12; 2023.

25.   contributors, P. *PDAL: The Point Data Abstraction Library*, 2022.

26.   contributors, D.O. *GDAL/OGR Geospatial Data Abstraction software Library*, Open Source Geospatial Foundation: 2022.

27.   Team, Q.D. *QGIS Geographic Information System*, Open Source Geospatial Foundation Project: 2002.

28.   Annan, A. GPR—History, trends, and future developments. *Subsurface sensing technologies and applications* **2002**, *3*, 253-270.

29.   Cui, X.; Guo, L.; Chen, J.; Chen, X.; Zhu, X. Estimating tree-root biomass in different depths using ground-penetrating radar: Evidence from a controlled experiment. *IEEE Transactions on Geoscience and Remote Sensing* **2012**, *51*, 3410-3423.

30.   Goodman, D. *GPR-SLICE Software*, Geophysical Archaeometry Lab Inc: Woodland Hills, CA, USA, 2016.

31.   R Development Core Team *R: A language and environment for statistical computing*, 4.2.2; R Foundation for Statistical Computing: 2023.

32.   Rouse, J.W.; Haas, R.H.; Schell, J.A.; Deering, D.W. Monitoring vegetation systems in the Great Plains with ERTS. *NASA Spec. Publ* **1974**, *351*, 309.

33.   Breiman, L. Random forests. *Machine learning* **2001**, *45*, 5-32.

34.   Sharma, P.; Leigh, L.; Chang, J.; Maimaitijiang, M.; Caffé, M. Above-ground biomass estimation in oats using UAV remote sensing and machine learning. *Sensors* **2022**, *22*, 601.

35.   Popescu, S.C. Estimating biomass of individual pine trees using airborne lidar. *Biomass and Bioenergy* **2007**, *31*, 646-655.

36.   Kang, Y.; Meng, Q.; Liu, M.; Zou, Y.; Wang, X. Crop classification based on red edge features analysis of GF-6 WFV data. *Sensors* **2021**, *21*, 4328.

37.   Horler, D.; DOCKRAY, M.; Barber, J. The red edge of plant leaf reflectance. *International journal of remote sensing* **1983**, *4*, 273-288.

38.   Hosoi, F.; Omasa, K. Estimating vertical plant area density profile and growth parameters of a wheat canopy at different growth stages using three-dimensional portable lidar imaging. *ISPRS Journal of Photogrammetry and Remote Sensing* **2009**, *64*, 151-158.

39.   Ehlert, D.; Adamek, R.; Horn, H.-J. Laser rangefinder-based measuring of crop biomass under field conditions. *Precision Agriculture* **2009**, *10*, 395-408.

40.   Long, D.S.; McCallum, J.D. Mapping straw yield using on-combine light detection and ranging (lidar). *International journal of remote sensing* **2013**, *34*, 6121-6134.

41.   Asner, G.P.; Levick, S.R.; Kennedy-Bowdoin, T.; Knapp, D.E.; Emerson, R.; Jacobson, J.; Colgan, M.S.; Martin, R.E. Large-scale impacts of herbivores on the structural diversity of African savannas. *Proceedings of the National Academy of Sciences* **2009**, *106*, 4947-4952.